

Flat Electron Bands with Bad Valley Quantum Numbers in Twisted Bi-Layer Graphene

J.P. Rodriguez

Department of Physics and Astronomy, California State University, Los Angeles,
California 90032, USA

E-mail: jrodrig@calstatela.edu

August 2017

Abstract. We compute the energy spectrum of a nearest-neighbor electron hopping model for bi-layer graphene at commensurate twist angles. Specifically, we focus on the simplest bi-layer lattices, with moiré patterns that have no subcells. The electron hopping hamiltonian is analyzed in momentum space, both by degenerate perturbation theory and by exact numerical calculation. We find that the degeneracy in energy along the edge of the moiré Brillouin zone due to the two valley quantum numbers is noticeably broken in the flat central bands at the magic twist angle. A mechanism for the appearance of flat central bands themselves at the magic twist angle is also revealed. It is due to maximal level repulsion. The mechanism relies on the assumption that the phase factor for the AA hamiltonian matrix element for inter-graphene-sheet hopping at the middle of the edge of the moiré Brillouin zone has a phase equal to half the twist angle. This assumption is confirmed in the case of uniform AA hopping in between the two sheets of graphene, in the limit of large moiré unit cells.

1. Introduction

It is well known that electron-electron correlations can lead to insulating behavior in systems with unfilled bands. This is the case, for example, in copper-oxides, where high-temperature superconductivity emerges after doping the correlated (Mott) insulator state with holes. Similar behavior has been observed recently in bi-layer graphene at a magic twist angle of $\theta = 1.08^\circ$. Superconductivity has been observed at a hole doping just beyond $\nu = -2$ electrons per moiré unit cell[1]. And a correlated insulator state has been observed at $\nu = -2$ electrons per moiré unit cell, as well as at $\nu = 2$ [2]. This observation of superconductivity upon hole-doping the half-filled hole bands in bi-layer graphene at the magic twist angle was quickly reproduced by other groups[3][4].

That flat electron bands in twisted bi-layer graphene exist at the magic angle was predicted theoretically a decade before the experimental discovery noted above[5][6][7]. In particular, these numerical calculations found that the velocity of the Dirac cones near charge neutrality is strongly renormalized down at the magic twist angle. A fundamental understanding of this effect remains unknown, however.

In this paper, we study the electronic properties of bi-layer graphene at commensurate twist angles on the basis of a nearest-neighbor electron hopping model. We primarily focus on commensurate twists that produce periodic moiré patterns with no subcells. These result in the smallest number of carbon atoms per true moiré unit cell. Degenerate perturbation theory reveals inter-valley mixing at the corners of the moiré Brillouin zone. Direct calculation finds, however, that the corresponding matrix element is small by a factor of one-over a quarter of the number of carbon atoms per true moiré unit cell. Importantly, this result agrees with the popular twist construction of the reciprocal lattice introduced by Bistritzer and MacDonald[7], which neglects such transitions. Both degenerate perturbation theory and exact numerical calculation find that valley degeneracy of the energy spectrum is broken near the corners of the moiré Brillouin zone. Specifically, exact numerical calculation reveals that the breaking of valley degeneracy becomes apparent in the dispersion of the flat central energy bands at the magic twist angle along the edge of the moiré Brillouin zone.

Following the Bistritzer-MacDonald twist construction[7], on the other hand, we apply degenerate perturbation theory at the middle of the edge of the moiré Brillouin zone. We find that flat bands exist at the magic twist angle because of maximal level repulsion there. This result relies on the assumption that the phase factor of the corresponding inter-valley matrix element between A sites there has a phase equal to half the twist angle. This assumption is corroborated in the case of uniform nearest-neighbor electron hopping in between the two sheets of graphene, in the limit of large moiré unit cells.

The paper is organized as follows. Section 2 describes the nature of the lattice of bi-layer graphene at commensurate twist angles, while the nature of the corresponding reciprocal lattice, which is dual to former, is described in section 3. The nearest-neighbor hopping hamiltonian is analyzed in section 4, where the flat-band effect is revealed. Last,

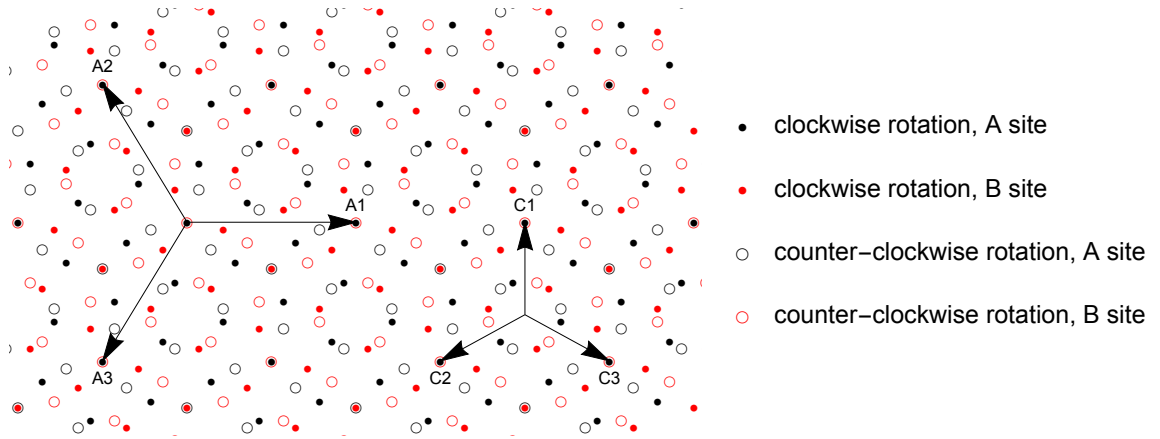


Figure 1. Bi-layer graphene at the largest commensurate twist angle: $\theta = 21.8^\circ$. It has integer parameters $m = 2$ and $n = 1$, with $l = 7$ A(B) sites per moiré unit cell, per sheet of graphene. [See Eqs. (1) and (2).]

exact dispersions of the flat bands at the magic twist angle are computed numerically in section 5.

2. Bi-Layer Honeycomb Lattices at Commensurate Twist Angles

Consider bi-layer graphene with no twist. It exhibits Bernal stacking, with A sites on top of B sites, and vice versa. Figure 1 shows a commensurate bi-layer that twists about such Bernal stacks, with the maximum twist angle of $\theta = 21.8^\circ$. It notably shows three types of twist centers: Bernal stacks with A sites on top of B sites, and vice versa, and twist centers with rings of nearest-neighbor A sites in between graphene sheets and nearest-neighbor B sites in between graphene sheets. We will show below that an infinite series of such commensurate twisted bi-layer graphene lattices exist with smaller twist angles that approach zero.

We start from bi-layer graphene in the Bernal-stacked form, with *no* twist. The (redundant) primitive vectors among the A(B) sites are: $\mathbf{a}_1 = a_\Delta \hat{\mathbf{y}}$, $\mathbf{a}_2 = a_\Delta (-\frac{\sqrt{3}}{2} \hat{\mathbf{x}} - \frac{1}{2} \hat{\mathbf{y}})$, and $\mathbf{a}_3 = a_\Delta (\frac{\sqrt{3}}{2} \hat{\mathbf{x}} - \frac{1}{2} \hat{\mathbf{y}})$. Here, $a_\Delta = \sqrt{3}a$ is the lattice constant, where a is the carbon-carbon separation in graphene. Now let m and n be positive integers that are relatively prime, with $m > n$, and consider the following pair of displacements from a Bernal stacking[6][8][9]: $\mathbf{A}_1(+)$ = $-m\mathbf{a}_2 + n\mathbf{a}_3$ from the A site of the stack, $\mathbf{A}_1(-)$ = $-n\mathbf{a}_2 + m\mathbf{a}_3$ from the B site of the stack. They are related to each other through a reflection about the x axis. We can then create a commensurate lattice by twisting the graphene sheet that contains the A site of the stack clockwise by an appropriate angle α , and by twisting the other graphene sheet that contains the B site of the stack counterclockwise by the same angle α , such that the two displacements coincide at a new Bernal stack. Because the difference in the two displacement vectors is $\mathbf{A}_1(+)-\mathbf{A}_1(-) = (m-n)\mathbf{a}_1$, while the magnitude of each displacement vector is

$|\mathbf{A}_1(\pm)| = (m^2 + mn + n^2)^{1/2}a_\Delta$, we have that the equal and opposite twist angle α satisfies

$$2 \sin \alpha = (m - n)/\sqrt{l}, \quad (1)$$

where

$$l = m^2 + mn + n^2 \quad (2)$$

is the number of A(B) sites per *true* moiré unit cell, per sheet of graphene. Upon such an equal and opposite twist, a triangular lattice of Bernal stacks is achieved, with (redundant) moiré primitive vectors

$$\mathbf{A}_1 = \sqrt{l}a_\Delta \hat{\mathbf{x}}, \quad \mathbf{A}_2 = \sqrt{l}a_\Delta \left(-\frac{1}{2}\hat{\mathbf{x}} + \frac{\sqrt{3}}{2}\hat{\mathbf{y}} \right), \quad \mathbf{A}_3 = \sqrt{l}a_\Delta \left(-\frac{1}{2}\hat{\mathbf{x}} - \frac{\sqrt{3}}{2}\hat{\mathbf{y}} \right), \quad (3)$$

Repeating the previous, but swapping the A and B sites of the Bernal stacks, results in another moiré triangular lattice. We will show below that the two sets of Bernal stacks form a honeycomb lattice if $m - n$ is not a multiple of 3.

Again consider untwisted bi-layer graphene, but with the less common AA stacking instead. Designate a center of one honeycomb cell as a new twist center. From that center, the A sites of the honeycomb lattice have (redundant) basis vectors: $\mathbf{c}_1 = a\hat{\mathbf{x}}$, $\mathbf{c}_2 = a(-\frac{1}{2}\hat{\mathbf{x}} + \frac{\sqrt{3}}{2}\hat{\mathbf{y}})$, and $\mathbf{c}_3 = a(-\frac{1}{2}\hat{\mathbf{x}} - \frac{\sqrt{3}}{2}\hat{\mathbf{y}})$. Consider next an A(B) site in one sheet of graphene that is displaced from the designated twist center by $\mathbf{C}_1(+)=m\mathbf{c}_2-n\mathbf{c}_3$, and a B(A) site in the other sheet of graphene that is displaced from the designated twist center by $\mathbf{C}_1(-)=n\mathbf{c}_2-m\mathbf{c}_3$. The magnitude of each displacement vector is $|\mathbf{C}_1(\pm)| = (m^2 + mn + n^2)^{1/2}a$. Recall now that given a general displacement from the center $p\mathbf{c}_2 + q\mathbf{c}_3$, where p and q are integers, then it is an A site for $(p+q) \bmod 3 = 1$, a B site for $(p+q) \bmod 3 = 2$, and a center of a honeycomb cell for $(p+q) \bmod 3 = 0$. Yet the difference of the two displacements above is $\mathbf{C}_1(-) - \mathbf{C}_1(+) = (m-n)\mathbf{c}_1$. We then conclude that twisting the graphene sheet with the A(B) displacement $\mathbf{C}_1(+)$ clockwise by the angle (1) α , and twisting the graphene sheet with the B(A) displacement $\mathbf{C}_1(-)$ counterclockwise by the angle α results in a Bernal stack if $m-n$ is *not* a multiple of 3. Such a twist applied to the displacements $-\mathbf{C}_1(\pm)$ results in another Bernal stack, but with the A site and B site swapped. The twist of each graphene sheet clockwise and counterclockwise by the angle α thereby results in a moiré honeycomb of Bernal stacks when $m-n$ is not a multiple of 3. The displacement vectors of the Bernal stacks of the resulting twisted bi-layer graphene lattice from the twisted AA stacking center above are

$$\mathbf{C}_1 = \sqrt{l}a\hat{\mathbf{y}}, \quad \mathbf{C}_2 = \sqrt{l}a \left(-\frac{\sqrt{3}}{2}\hat{\mathbf{x}} - \frac{1}{2}\hat{\mathbf{y}} \right), \quad \mathbf{C}_3 = \sqrt{l}a \left(\frac{\sqrt{3}}{2}\hat{\mathbf{x}} - \frac{1}{2}\hat{\mathbf{y}} \right). \quad (4)$$

They are shown in Fig. 1. Last, the case when $(m-n) \bmod 3 = 0$ coincides with a triangular lattice of Bernal stacks of the same type: for example, all A site of graphene

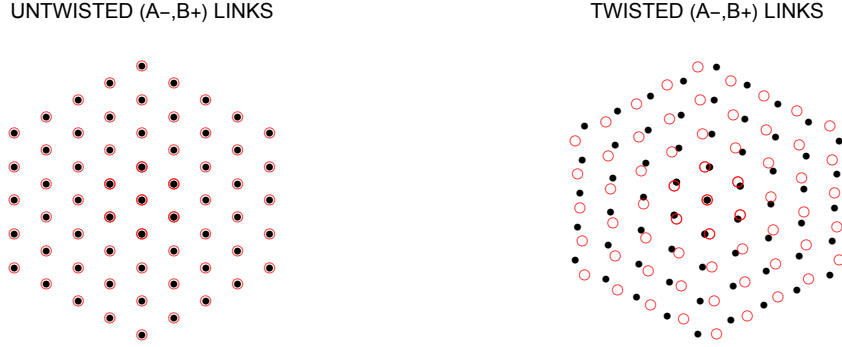


Figure 2. Nearest neighbor links within a moiré unit cell between A sites in clockwise-rotated sheet of graphene (black dot) and B sites in counterclockwise-rotated sheet of graphene (red circle) for the case of $n = 4$ consecutive hexagonal shells, plus the twist center ($m = 5$). It corresponds to $l = 61$ A(B) sites in each moiré unit cell per sheet of graphene. The commensurate twist angle is equal to $\theta = 7.3^\circ$.

sheet rotated counterclockwise over B site of graphene sheet rotated clockwise, or vice versa.

We shall next determine the nearest-neighbors between two sheets of graphene upon a commensurate twist, as just described. Let us confine ourselves hereafter to the case where $m = n + 1$, which we name the Periodic Moiré Pattern line. The true Wigner-Seitz unit cell has no moiré subcells in such case. (Cf. Fig. 12.) The number of A(B) sites per graphene sheet, per moiré unit cell, (2) is then equal to $l = 1 + 3n(n + 1)$ in such case. If we start from a Bernal stack in untwisted bi-layer graphene, the moiré unit cell then corresponds to n consecutive hexagonal shells of A and B sites in each respective sheet of graphene. Adding the twist center yields the total number of nearest-neighbor links inside the moiré unit cell between A sites in the minus-rotated sheet of graphene and B sites in the plus-rotated sheet, l . This is shown in Fig. 2 for the case $n = 4$ and $m = 5$, which has $l = 61$ A(B) sites in each moiré unit cell per sheet of graphene. The sites corresponding to twisted bi-layer graphene are achieved by twisting the respective sheets of graphene clockwise and counterclockwise by the angle (1) α about the Bernal stack at the center of the hexagonal shells. See, again, Fig. 2.

Nearest-neighbor A sites between graphene sheets are shown in Fig. 3. The twist center is located at the center of the super-honeycomb cells formed by the Bernal stacks. (See Fig. 1.) As in the previous case, there exist n hexagonal shells, with the exception that the smallest shell forms a triangle. There is no A site at the twist center, however. And because inter-graphene-sheet links with an A site at a Bernal stack are excluded, the number of such nearest-neighbor links inside a moiré unit cell is $l - 1 = 3n(n + 1)$. Direct summation of the number of such A-A matrix elements inside a moiré unit cell confirms this result. (See Appendix C.1.) Last, the corresponding B sites are obtained by simple space inversion of the A sites about the twist center.

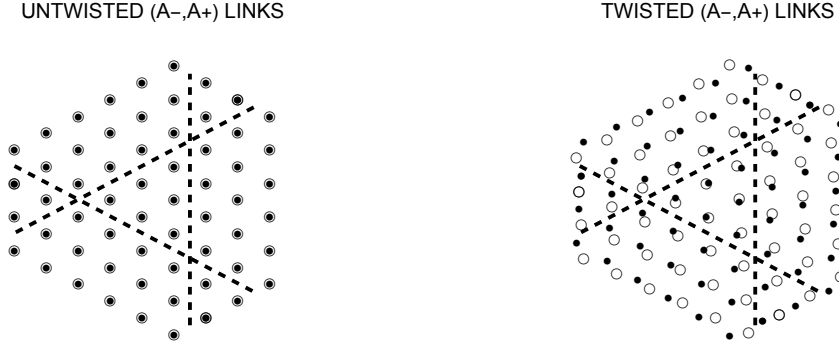


Figure 3. Nearest neighbor links within a moiré unit cell between A sites in clockwise-rotated sheet of graphene (black dot) and A sites in counterclockwise-rotated sheet of graphene (black circle). The commensurate twist angle is equal to $\theta = 7.3^\circ$. It corresponds to integer parameters $m = 5$ and $n = 4$, with $l = 61$ A(B) sites per moiré unit cell, per sheet of graphene.

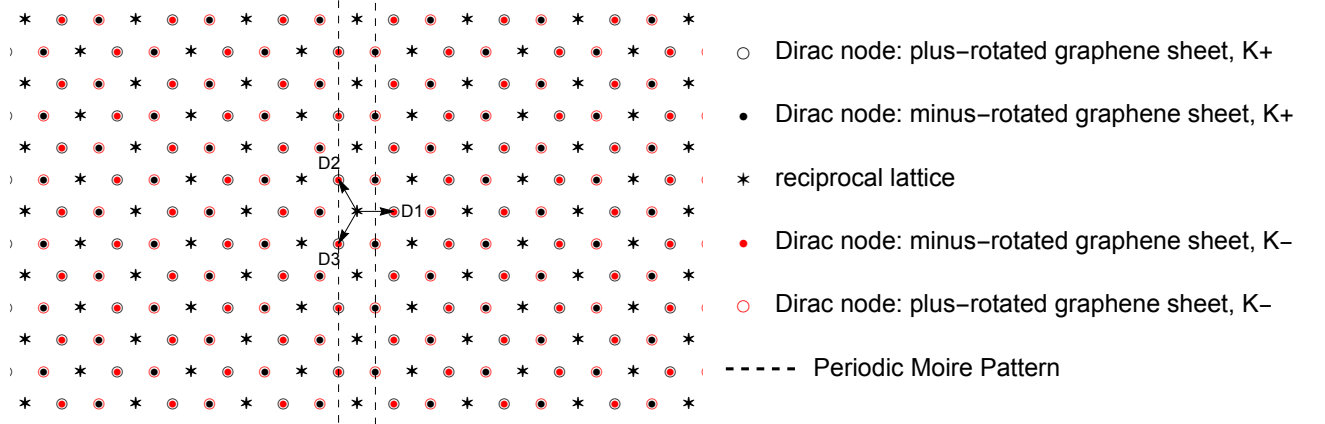


Figure 4. Moiré reciprocal lattice (*) of bi-layer graphene and the Dirac nodes corresponding to the minus-rotated (●) and plus-rotated (○) sheets of graphene at commensurate twist angles.

3. Bloch Theorem

Below, we shall construct the hamiltonian for an electron hopping in between nearest neighbors in twisted bi-layer graphene at commensurate twist angles, e.g. Fig. 1, but in momentum space.

3.1. Momentum Space

The (redundant) primitive vectors of the moiré reciprocal lattice can be obtained from the primitive vectors of the moiré lattice (3), and they are

$$\mathbf{B}_1 = \frac{2\pi}{\sqrt{l}d}\hat{\mathbf{y}}, \quad \mathbf{B}_2 = \frac{2\pi}{\sqrt{l}d}\left(-\frac{\sqrt{3}}{2}\hat{\mathbf{x}} - \frac{1}{2}\hat{\mathbf{y}}\right), \quad \mathbf{B}_3 = \frac{2\pi}{\sqrt{l}d}\left(\frac{\sqrt{3}}{2}\hat{\mathbf{x}} - \frac{1}{2}\hat{\mathbf{y}}\right), \quad (5)$$

where $d = \frac{\sqrt{3}}{2}a_\Delta = \frac{3}{2}a$ is the shortest distance in between Bragg planes of A(B) sites

in graphene. Figure 4 shows the resulting reciprocal lattice. It is well known that momentum space is *inverted* by comparison with real space. For example, by comparison with the moiré primitive vectors (3) \mathbf{A}_1 , \mathbf{A}_2 , and \mathbf{A}_3 ,

$$\mathbf{b}_1(+) = -m\mathbf{B}_2 + n\mathbf{B}_3 \quad \text{and} \quad \mathbf{b}_1(-) = -n\mathbf{B}_2 + m\mathbf{B}_3 \quad (6)$$

give the first primitive vectors of the plus-rotated and minus-rotated reciprocal lattices of the respective sheets of graphene. Their un-rotated counterparts are

$$\mathbf{b}_1 = \frac{2\pi}{d}\hat{\mathbf{x}}, \quad \mathbf{b}_2 = \frac{2\pi}{d}\left(-\frac{1}{2}\hat{\mathbf{x}} + \frac{\sqrt{3}}{2}\hat{\mathbf{y}}\right), \quad \mathbf{b}_3 = \frac{2\pi}{d}\left(-\frac{1}{2}\hat{\mathbf{x}} - \frac{\sqrt{3}}{2}\hat{\mathbf{y}}\right). \quad (7)$$

Likewise, by comparison with the displacement vectors \mathbf{C}_1 , \mathbf{C}_2 , and \mathbf{C}_3 , in twisted bi-layer graphene (Fig. 1), the Dirac nodes in the counter-clockwise-rotated sheet of graphene and in the clockwise-rotated sheet of graphene are related to moiré Dirac nodes by

$$\mathbf{d}_1(+) = m\mathbf{D}_2 - n\mathbf{D}_3 \quad \text{and} \quad \mathbf{d}_1(-) = n\mathbf{D}_2 - m\mathbf{D}_3. \quad (8)$$

Here,

$$\mathbf{D}_1 = \frac{K}{\sqrt{l}}\hat{\mathbf{x}}, \quad \mathbf{D}_2 = \frac{K}{\sqrt{l}}\left(-\frac{1}{2}\hat{\mathbf{x}} + \frac{\sqrt{3}}{2}\hat{\mathbf{y}}\right), \quad \mathbf{D}_3 = \frac{K}{\sqrt{l}}\left(-\frac{1}{2}\hat{\mathbf{x}} - \frac{\sqrt{3}}{2}\hat{\mathbf{y}}\right), \quad (9)$$

are moiré Dirac nodes that are closest to the zero reciprocal lattice vector, as shown in Fig. 4, while

$$\mathbf{d}_1 = K\hat{\mathbf{y}}, \quad \mathbf{d}_2 = K\left(-\frac{\sqrt{3}}{2}\hat{\mathbf{x}} - \frac{1}{2}\hat{\mathbf{y}}\right), \quad \mathbf{d}_3 = K\left(\frac{\sqrt{3}}{2}\hat{\mathbf{x}} - \frac{1}{2}\hat{\mathbf{y}}\right), \quad (10)$$

are the Dirac nodes of an un-rotated sheet of graphene. Above, $K = 4\pi/3a_\Delta$ is the lattice constant of the honeycomb of such Dirac nodes.

Now notice by (8) that the twist in the location of the Dirac node at \mathbf{d}_1 results in the difference $\mathbf{d}_1(-) - \mathbf{d}_1(+) = (m - n)\mathbf{D}_1$. By expression (9) for \mathbf{D}_1 , the twist angle $2\sin\alpha = |\mathbf{d}_1(-) - \mathbf{d}_1(+)|/K$ thereby coincides with the formula (1) obtained in real space. At integer parameters $m - n = 1$, the reciprocal lattice of the bi-layer graphene at commensurate twist coincides with the twist construction of the reciprocal lattice introduced by Bistritzer and MacDonald [7]. In that case, for example, the lattice constant of the moiré Dirac nodes shown in Fig. 4 is related to the lattice constant of the Dirac nodes in an isolated sheet of graphene by

$$K_M = 2(\sin\alpha)K. \quad (11)$$

The resulting moiré pattern is thereby periodic[5]. Henceforth, we shall therefore call the constraint $m - n = 1$ the Periodic Moiré Pattern line. For integer parameters along the Periodic Moiré Pattern line, the Dirac nodes $\mathbf{d}_1(+)$ and $\mathbf{d}_1(-)$ for the plus-rotated and minus-rotated sheets of graphene, respectively, lie along the left dashed line and the right dashed line that are shown in Fig. 4. Figure 5 shows the moiré reciprocal lattice plus the Dirac nodes corresponding to each sheet of graphene in the case of integer parameters $m = 5$ and $n = 4$. It has $l = 61$ A(B) sites per sheet of graphene in a moiré unit cell. Notice that the first Brillouin zone for each sheet of graphene contain

$n = 4$ consecutive hexagonal shells of moiré reciprocal lattice vectors that surround the central one. This is generally true along the Periodic Moiré Pattern line. Indeed, the number of moiré reciprocal lattice vectors in n consecutive hexagonal shells that start from a central reciprocal lattice vector is $3n(n+1)$, which by (2) is precisely $l-1$ when $m = n+1$.

Last, let us discuss the periodic boundary conditions, to be assumed hereafter. The spatial periods shall be $\mathbf{L}_1 = N_1 \mathbf{A}_1$ and $\mathbf{L}_2 = N_2 \mathbf{A}_2$, where N_1 and N_2 are positive integers. Recall the identities $\mathbf{B}_i \cdot \mathbf{A}_{\bar{j}} = (-1)^{i-1} 2\pi \delta_{i,j}$, where $\bar{1} = 2$ and $\bar{2} = 1$. An allowed wavenumber \mathbf{k} must satisfy $e^{i\mathbf{k} \cdot \mathbf{L}_1} = 1 = e^{i\mathbf{k} \cdot \mathbf{L}_2}$. This yields that the allowed wave numbers are

$$\mathbf{k} = \frac{n_1}{N_2} \mathbf{B}_1 + \frac{n_2}{N_1} \mathbf{B}_2, \quad (12)$$

where n_1 and n_2 are any integers.

3.2. Electron Hopping Hamiltonian

We shall model the electronic structure of twisted bi-layer graphene at commensurate twist angles by electron hopping within (\parallel) and in between (\perp) the twisted sheets of graphene. The nearest neighbors within each sheet of graphene are consecutive A and B sites on the honeycomb, while nearest neighbors in between twisted sheets of graphene are achieved by twisting A/B and A/A stacked bi-layer graphene. Figures 2 and 3 show this, respectively. The matrix element for electron hopping between nearest-neighbors in graphene is called $-t_{\parallel}$, while the matrix element for a nearest-neighbor link in between twisted sheets of graphene is called $-t_{\perp}^{(0)}$ or $-t_{\perp}^{(1)}$. Here, the superscript 0 refers to A-A or B-B links, while the superscript 1 refers to A-B or B-A links.

The intra-graphene-sheet contribution to the hamiltonian of an electron with crystal momentum \mathbf{k} is $H_{++}(\mathbf{k}) + H_{--}(\mathbf{k})$, where

$$H_{\pm\pm}(\mathbf{k}) = -t_{\parallel} \sum_{i=0}^{l-1} [\zeta_{\pm}(\mathbf{k} - \mathbf{G}_i) |\mathbf{k} - \mathbf{G}_i, A, \pm\rangle \langle \mathbf{k} - \mathbf{G}_i, B, \pm| + \text{H.C.}]. \quad (13)$$

Here, the quantum numbers $+$ and $-$ denote the $+\alpha$ -rotated and $-\alpha$ -rotated sheets of graphene, respectively, while $\mathbf{G}_0, \mathbf{G}_1, \dots, \mathbf{G}_{l-1}$ are the moiré reciprocal lattice vectors that lie inside the first Brillouin zone of a twisted sheet of graphene in isolation. Figure 5 shows these in the case of $l = 61$ A(B) sites per sheet of graphene in a moiré unit cell. The l moiré reciprocal lattice vectors are common to both sheets of graphene! The null reciprocal lattice vector is \mathbf{G}_0 . Above, also,

$$\zeta_{\pm}(\mathbf{k}) = e^{i\mathbf{k} \cdot \mathbf{c}_1(\pm)} + e^{i\mathbf{k} \cdot \mathbf{c}_2(\pm)} + e^{i\mathbf{k} \cdot \mathbf{c}_3(\pm)} \quad (14)$$

is the standard phase factor of the A-to-B site matrix element in graphene. The hamiltonian (13) is expressed in terms of plane-wave states

$$|\mathbf{k}, A(B), \pm\rangle = \frac{1}{N^{1/2}} \sum_{\mathbf{r}_{A(B)\pm}} e^{i\mathbf{k} \cdot \mathbf{r}_{A(B)\pm}} |\mathbf{r}_{A(B)\pm}, A(B), \pm\rangle, \quad (15)$$

where $N = l \cdot N_M$ is the total number of A(B) sites, $\mathbf{r}_{A(B)\pm}$, in the $\pm\alpha$ -rotated sheet of graphene, with $N_M = N_1 N_2$ true moiré unit cells. Above, $|\mathbf{r}_{A(B)\pm}, A(B), \pm\rangle$ is a site state in twisted bi-layer graphene.

In real space, the inter-graphene-sheet contribution to the hamiltonian of an electron has the form $H_{-+} + H_{+-}$, where H_{-+} has four components:

$$\begin{aligned} H_{A-,A+} &= - \sum_{\delta\mathbf{r}_{A/A}} \sum_{\mathbf{R}} t_{\perp}^{(0)} |\mathbf{R} + \delta\mathbf{r}_{A/A}(-), A, -\rangle \langle \mathbf{R} + \delta\mathbf{r}_{A/A}(+), A, +| \\ H_{A-,B+} &= - \sum_{\delta\mathbf{r}_{B/A}} \sum_{\mathbf{R}} t_{\perp}^{(1)} |\mathbf{R} + \mathbf{C}_3 + \delta\mathbf{r}_{B/A}(-), A, -\rangle \langle \mathbf{R} + \mathbf{C}_3 + \delta\mathbf{r}_{B/A}(+), B, +| \\ H_{B-,A+} &= - \sum_{\delta\mathbf{r}_{A/B}} \sum_{\mathbf{R}} t_{\perp}^{(1)} |\mathbf{R} - \mathbf{C}_2 + \delta\mathbf{r}_{A/B}(-), B, -\rangle \langle \mathbf{R} - \mathbf{C}_2 + \delta\mathbf{r}_{A/B}(+), A, +| \\ H_{B-,B+} &= - \sum_{\delta\mathbf{r}_{B/B}} \sum_{\mathbf{R}} t_{\perp}^{(0)} |\mathbf{R} + \delta\mathbf{r}_{B/B}(-), B, -\rangle \langle \mathbf{R} + \delta\mathbf{r}_{B/B}(+), B, +|. \end{aligned} \quad (16)$$

Above, \mathbf{R} denote the twist centers for A-A and B-B nearest-neighbor links in between sheets of graphene per true moiré unit cell, which are shown by Fig. 1. The displacements $\delta\mathbf{r}_{A/A}(+)$ and $\delta\mathbf{r}_{A/A}(-)$, for example, denote the plus-rotated A site of the A-A link and the minus-rotated A site of the A-A link in comparison to the A/A twist center. (See Fig. 3.) And notice that $\delta\mathbf{r}_{B/B}(\pm) = -\delta\mathbf{r}_{A/A}(\pm)$. Also, the displacements $\delta\mathbf{r}_{B/A}(+)$ and $\delta\mathbf{r}_{B/A}(-)$, for example, denote the plus-rotated B site of the B-A link and the minus-rotated A site of the B-A link in comparison to the B/A twist center. (See Fig. 2.) The displacement \mathbf{C}_3 of the latter twist center compared to the former twist center must be added in this case. Also notice that $\delta\mathbf{r}_{A/B}(\pm) = \delta\mathbf{r}_{B/A}(\pm)$. The displacement $-\mathbf{C}_2$ of this last twist center compared to the first twist center must be added in this case. Last, $H_{+-}(\mathbf{k})$ is the hermitian conjugate of (16) $H_{-+}(\mathbf{k})$.

To determine inter-graphene-sheet matrix elements of the hopping hamiltonian of the electron with crystal momentum \mathbf{k} , $H_{-+}(\mathbf{k})$, we substitute the inversion formula

$$|\mathbf{r}_{A(B)\pm}, A(B), \pm\rangle = \frac{1}{N^{1/2}} \sum_{\mathbf{k}} e^{-i\mathbf{k} \cdot \mathbf{r}_{A(B)\pm}} |\mathbf{k}, A(B), \pm\rangle \quad (17)$$

for the plane-wave states (15) into (16). This yields the respective matrix elements:

$$\begin{aligned} \langle\langle \mathbf{k}_i, A, - | H | \mathbf{k}_j, A, + \rangle\rangle &= - \sum_{\delta\mathbf{r}_{A/A}} \frac{t_{\perp}^{(0)}}{l} e^{i[-\mathbf{k}_i \cdot \delta\mathbf{r}_{A/A}(-) + \mathbf{k}_j \cdot \delta\mathbf{r}_{A/A}(+)]} \\ \langle\langle \mathbf{k}_i, A, - | H | \mathbf{k}_j, B, + \rangle\rangle &= - e^{i(\mathbf{G}_i - \mathbf{G}_j) \cdot \mathbf{C}_3} \sum_{\delta\mathbf{r}_{B/A}} \frac{t_{\perp}^{(1)}}{l} e^{i[-\mathbf{k}_i \cdot \delta\mathbf{r}_{B/A}(-) + \mathbf{k}_j \cdot \delta\mathbf{r}_{B/A}(+)]} \\ \langle\langle \mathbf{k}_i, B, - | H | \mathbf{k}_j, A, + \rangle\rangle &= - e^{-i(\mathbf{G}_i - \mathbf{G}_j) \cdot \mathbf{C}_2} \sum_{\delta\mathbf{r}_{A/B}} \frac{t_{\perp}^{(1)}}{l} e^{i[-\mathbf{k}_i \cdot \delta\mathbf{r}_{A/B}(-) + \mathbf{k}_j \cdot \delta\mathbf{r}_{A/B}(+)]} \\ \langle\langle \mathbf{k}_i, B, - | H | \mathbf{k}_j, B, + \rangle\rangle &= - \sum_{\delta\mathbf{r}_{B/B}} \frac{t_{\perp}^{(0)}}{l} e^{i[-\mathbf{k}_i \cdot \delta\mathbf{r}_{B/B}(-) + \mathbf{k}_j \cdot \delta\mathbf{r}_{B/B}(+)]}, \end{aligned} \quad (18)$$

where $\mathbf{k}_i = \mathbf{k} - \mathbf{G}_i$ and $\mathbf{k}_j = \mathbf{k} - \mathbf{G}_j$. Notice that $\mathbf{k}_i - \mathbf{k}_j$ is a moiré reciprocal lattice vector, $\mathbf{G}_j - \mathbf{G}_i$. Also, the matrix elements that correspond to $H_{+-}(\mathbf{k})$ are the hermitian

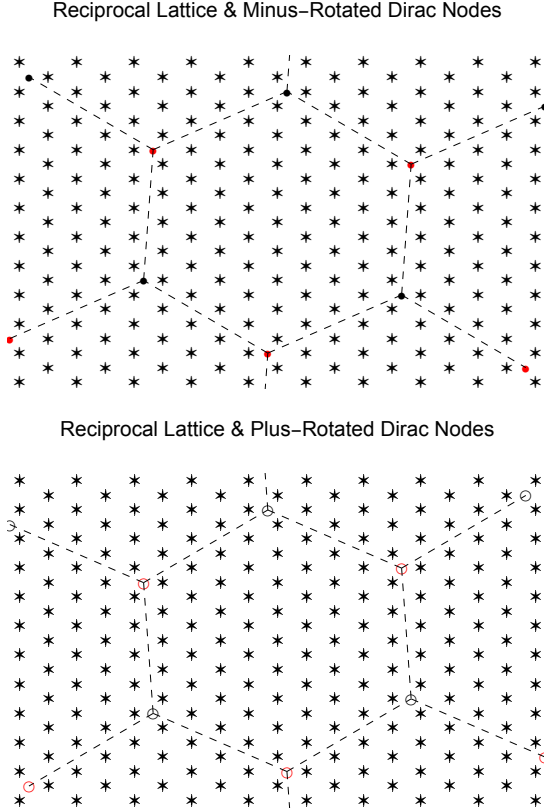


Figure 5. Moiré reciprocal lattice (*) of bi-layer graphene at commensurate twist angle equal to $\theta = 7.3^\circ$, which corresponds to integer parameters $m = 5$ and $n = 4$. Also shown are the Dirac nodes corresponding to the minus-rotated (·-) and plus-rotated (·+) sheets of graphene. The dashed lines represent the edge of the first Brillouin zone of the rotated sheets of graphene. Both Brillouin zones of the graphene sheets in isolation contain $l = 61$ moiré reciprocal lattice vectors.

conjugates of the above. This can be seen explicitly by swapping the $-$ and $+$ twist-layer quantum numbers in (18).

The phase factors appearing in the off-diagonal A/B and B/A matrix elements (18) are easily calculated. Let $\mathbf{G} = n_1 \mathbf{B}_1 + n_2 \mathbf{B}_2$ be a moiré reciprocal lattice vector, where n_1 and n_2 are integers. A direct calculation using expressions (4) and (5) yields the phase factor $e^{i\mathbf{G} \cdot \mathbf{C}_1} = (e^{-i2\pi/3})^{n_1+n_2}$. The differences $\mathbf{C}_2 - \mathbf{C}_1 = \mathbf{A}_3$ and $\mathbf{C}_3 - \mathbf{C}_1 = -\mathbf{A}_2$ then yields that $e^{i\mathbf{G} \cdot \mathbf{C}_2}$ and $e^{i\mathbf{G} \cdot \mathbf{C}_3}$ are both equal to the previous result for $e^{i\mathbf{G} \cdot \mathbf{C}_1}$. Appendix A shows how a suitable gauge transformation removes the above phase factors from the off-diagonal A/B and B/A matrix elements (18), while they reappear in the corresponding A/A and B/B matrix elements. This becomes convenient in the chiral limit[10], where the latter matrix elements vanish.

We thereby conclude the construction of the electron hopping hamiltonian in momentum space. It has the form

$$H(\mathbf{k}) = \begin{bmatrix} H_{--}(\mathbf{k}) & H_{-+}(\mathbf{k}) \\ H_{+-}(\mathbf{k}) & H_{++}(\mathbf{k}) \end{bmatrix}. \quad (19)$$

The intra-graphene-sheet parts (13), H_{--} and H_{++} , are 2×2 -block diagonal $2l \times 2l$

Out[]:=

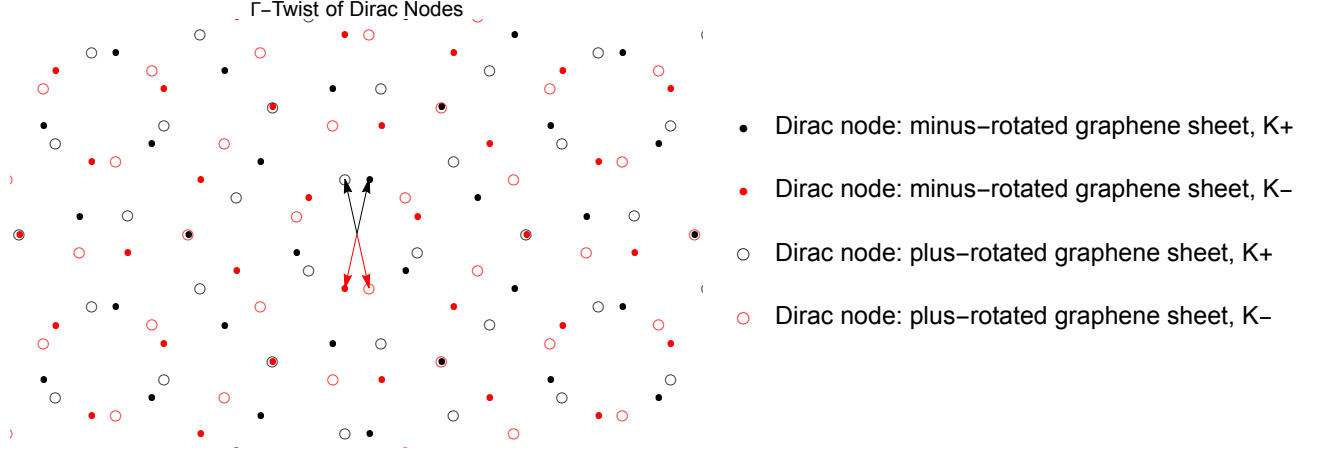


Figure 6. Dirac nodes of graphene sheets that are twisted about the common Γ point in the first Brillouin zone by the largest commensurate angle $\theta = 21.8^\circ$. It corresponds to integer parameters $m = 2$ and $n = 1$. The black arrows and red arrows highlight the twist at the $K+$ and $K-$ Dirac nodes of graphene, respectively. Comparison with Fig. 1 for the corresponding lattice in real space reveals *duality*: rotation by 90° .

matrices, while the inter-graphene-sheet parts (18), H_{-+} and H_{+-} , are dense $2l \times 2l$ matrices.

4. Degenerate Perturbation Theory

Figure 6 shows the Dirac nodes of bi-layer graphene twisted by a commensurate angle equal to $\theta = 21.8^\circ$ about a common Γ point in the first Brillouin zone. The lattice of Dirac nodes in momentum space is equivalent to the lattice in real space of twisted bi-layer graphene, Fig. 1, but rotated by 90° . In the absence of hopping between sheets of graphene, the lowest-energy states are states near the coincidence of Dirac nodes in each sheet, black dot in red circle, or red dot in black circle, which mix valley quantum numbers. Below, we shall apply degenerate perturbation theory to such states, and thereby reveal the latter. Following Bistritzer and MacDonald[7], low-energy degenerate states also exist at momenta that bisect the twisted K points in the first Brillouin zone. Below, we shall also apply degenerate perturbation theory to such states, and thereby reveal the appearance of flat bands at a magic twist angle.

4.1. Electron Energy Spectrum near Corner of Moiré Brillouin Zone

The valley quantum numbers mix in twisted bi-layer graphene at commensurate twist angles. Figure 6 shows the corresponding graphene nodes at the largest commensurate twist angle of $\theta = 21.8^\circ$. It is analogous to Fig. 1 for twisted bi-layer graphene in real space, but rotated by 90° . Here, the Γ point in the first Brillouin zone of graphene is the common twist center for the two sheets of graphene. In general, assume bi-layer graphene with a commensurate twist angle such that the difference of the integer

parameters $m - n$ is not a multiple 3. This gaurantees the three types of twist centers evident in Fig. 1. (See section 2.) By analogy with such twisted bi-layer graphene in real space, the momenta $-m\mathbf{d}_2(-) + n\mathbf{d}_3(-)$ (red dot) and $-n\mathbf{d}_2(+) + m\mathbf{d}_3(+)$ (black circle) coincide, for example, at a point along the x axis that we shall name $+K_{\bar{M}}\hat{\mathbf{x}}$ (red dot in black circle). It follows the scaling law $K_{\bar{M}} = \sqrt{l} K$, where l is given by (2). An isolated sheet of graphene has two types of Dirac nodes in the energy spectrum: Dirac nodes at $+K\hat{\mathbf{y}}$ up to a reciprocal lattice vector, which we label by $K+$, and Dirac nodes at $-K\hat{\mathbf{y}}$ up to a reciprocal lattice vector, which we label by $K-$. The $+\alpha$ -rotated Dirac nodes at $K+$ are degenerate with the $-\alpha$ -rotated Dirac nodes at $K-$ at this point in momentum space, $K_{\bar{M}}+$. Vice versa, the momenta $m\mathbf{d}_2(-) - n\mathbf{d}_3(-)$ (black dot) and $n\mathbf{d}_2(+) - m\mathbf{d}_3(+)$ (red circle) coincide, for example, at a point along the x axis $-K_{\bar{M}}\hat{\mathbf{x}}$ (black dot in red circle). The $+\alpha$ -rotated Dirac nodes at $K-$ are degenerate with the $-\alpha$ -rotated Dirac nodes at $K+$ at this point in momentum space, $K_{\bar{M}}-$.

In the limit of weak hopping in between the sheets of graphene, we can apply degenerate perturbation theory at momenta near the point $+K_{\bar{M}}\hat{\mathbf{x}}$ identified above. (See Fig. 6, red dot in black circle.) Recall the Hamiltonian in momentum space constructed previously in section 3.2: (19) with matrix elements (13) and (18). The twist about the Γ point depicted by Fig. 6 coincides with truncating the hopping hamiltonian to momenta $\mathbf{k}_i = \mathbf{k} - \mathbf{G} = \mathbf{k}_j$, where \mathbf{G} is a reciprocal lattice vector inside a graphene Brillouin zone. This yields a truncated 4×4 hamiltonian of the form

$$H_{K_{\bar{M}}+}(\delta\mathbf{k}) = \begin{bmatrix} 0 & z_-^* & w'_0 & w'_1 \\ z_- & 0 & w'_1 & w_0'^* \\ w_0'^* & w_1'^* & 0 & z_+ \\ w_1'^* & w'_0 & z_+^* & 0 \end{bmatrix}. \quad (20)$$

Here, we express the momentum as $\mathbf{k} - \mathbf{G} = K_{\bar{M}}\hat{\mathbf{x}} + \delta\mathbf{k}$. Above, we have intra-graphene matrix elements $z_{\pm} = -t_{\parallel}\zeta_{\pm}(\mathbf{k} - \mathbf{G})$ at momenta $\mathbf{k} - \mathbf{G}$ in the vicinity of $K_{\bar{M}}\hat{\mathbf{x}}$. It is convenient to re-write the phase factor (14) as $\zeta_{\pm}(\mathbf{k}) = e^{i\mathbf{k}\cdot\mathbf{c}_1(\pm)}\zeta'_{\pm}(\mathbf{k})$, where $\zeta'_{\pm}(\mathbf{k}) = 1 + e^{i\mathbf{k}\cdot[\mathbf{c}_2(\pm) - \mathbf{c}_1(\pm)]} + e^{i\mathbf{k}\cdot[\mathbf{c}_3(\pm) - \mathbf{c}_1(\pm)]}$, or equivalently by the identities $\mathbf{a}_1 = \mathbf{c}_2 - \mathbf{c}_3$, $\mathbf{a}_2 = \mathbf{c}_3 - \mathbf{c}_1$, and $\mathbf{a}_3 = \mathbf{c}_1 - \mathbf{c}_2$,

$$\zeta'_{\pm}(\mathbf{k}) = 1 + e^{-i\mathbf{k}\cdot\mathbf{a}_3(\pm)} + e^{i\mathbf{k}\cdot\mathbf{a}_2(\pm)}. \quad (21)$$

Because expression (21) is manifestly periodic over the reciprocal lattice of the \pm -rotated sheet of graphene, Fig. 6 indicates the equalities $\zeta'_+(\mathbf{k} - \mathbf{G}) = \zeta'_+(\mathbf{d}_1(+) + \delta\mathbf{k})$ and $\zeta'_-(\mathbf{k} - \mathbf{G}) = \zeta'_-(\mathbf{d}_1(-) + \delta\mathbf{k})$. Hence, we have the respective Dirac cones $\zeta'_+(\mathbf{d}_1(+) + \delta\mathbf{k}) \cong i\frac{3}{2}a(\delta k_x + i\delta k_y)e^{-i\alpha}$ and $\zeta'_-(\mathbf{d}_1(-) + \delta\mathbf{k}) \cong i\frac{3}{2}a(\delta k_x - i\delta k_y)e^{-i\alpha}$. Second, it is shown in Appendix B that the phase factor at the degeneracy momentum $K_{\bar{M}}\hat{\mathbf{x}}$ is a cube-root of unity: $e^{+iK_{\bar{M}}\hat{\mathbf{x}}\cdot\mathbf{c}_1(\pm)} = \exp[i2\pi(m+n)/3]$. We thereby obtain the following expressions for the intra-graphene matrix elements of the truncated hamiltonian (20):

$$\begin{aligned} z_- &= -v_D e^{i(\alpha-\delta)} i^* (\delta k_x + i\delta k_y), \\ z_+ &= -v_D e^{-i(\alpha-\delta)} i (\delta k_x + i\delta k_y). \end{aligned} \quad (22)$$

Here, $v_D = \frac{3}{2}at_{\parallel}$ is the velocity of a Dirac cone, and $\delta = 2\pi(m+n)/3$ is a 3-fold symmetric phase angle. Along the Periodic Moiré Pattern line, $m = n + 1$, the latter is equal to $\delta = 2\pi(2n+1)/3$, which implies $e^{i\delta} = e^{-i2\pi(n-1)/3}$.

Next, we shall compute the inter-graphene-sheet matrix element w'_1 of the truncated hamiltonian (20). It is given by the expression

$$\langle\langle \mathbf{k}_i, A, - | H | \mathbf{k}_i, B, + \rangle\rangle = - \sum_{\delta \mathbf{r}_{B/A}} \frac{t_{\perp}^{(1)}}{l} e^{-i\mathbf{k}_i \cdot [\delta \mathbf{r}_{B/A}(-) - \delta \mathbf{r}_{B/A}(+)]} \quad (23)$$

for inter-graphene-sheet matrix elements (18) at momenta $\mathbf{k}_i = \mathbf{k} - \mathbf{G}$ near $K_{\bar{M}}\hat{\mathbf{x}}$. Henceforth, we shall confine the integer parameters to the Periodic Moiré Pattern line, $m = n + 1$, in which case the A-B links form n consecutive hexagonal shells within the Wigner-Seitz unit cell centered at the A-B Bernal stack. (See Fig. 2.) Using $\delta \mathbf{r}_{B/A}(\pm) = n_1 \mathbf{a}_1(\pm) + n_2 \mathbf{a}_2(\pm)$, where n_1 and n_2 are integers, we have that the arguments of the oscillatory exponentials in (23) have the form imaginary i times $(K_{\bar{M}}\hat{\mathbf{x}} \cdot \delta \mathbf{a}_1)n_1 + (K_{\bar{M}}\hat{\mathbf{x}} \cdot \delta \mathbf{a}_2)n_2$, where

$$\begin{aligned} \delta \mathbf{a}_1 &= \mathbf{a}_1(+) - \mathbf{a}_1(-) = -a_{\Delta}(2 \sin \alpha) \hat{\mathbf{x}}, \\ \delta \mathbf{a}_2 &= \mathbf{a}_2(+) - \mathbf{a}_2(-) = a_{\Delta}(2 \sin \alpha) \left(\frac{1}{2} \hat{\mathbf{x}} - \frac{\sqrt{3}}{2} \hat{\mathbf{y}} \right), \\ \delta \mathbf{a}_3 &= \mathbf{a}_3(+) - \mathbf{a}_3(-) = a_{\Delta}(2 \sin \alpha) \left(\frac{1}{2} \hat{\mathbf{x}} + \frac{\sqrt{3}}{2} \hat{\mathbf{y}} \right). \end{aligned} \quad (24)$$

Recall, now, that $K_{\bar{M}} = \sqrt{l} K$ and $K = 4\pi/3a_{\Delta}$. Three-fold symmetric terms are grouped together by adding such oscillatory exponential terms with arguments proportional to $n_1 \delta \mathbf{a}_1 + n_2 \delta \mathbf{a}_2$, $n_1 \delta \mathbf{a}_2 + n_2 \delta \mathbf{a}_3$, and $n_1 \delta \mathbf{a}_3 + n_2 \delta \mathbf{a}_1$. After applying 6-fold rotation symmetry of the right-hand side of (23), and using the following results for the dot products,

$$\begin{aligned} K_{\bar{M}}\hat{\mathbf{x}} \cdot \delta \mathbf{a}_1 &= -4\pi/3, \\ K_{\bar{M}}\hat{\mathbf{x}} \cdot \delta \mathbf{a}_2 &= +2\pi/3, \\ K_{\bar{M}}\hat{\mathbf{x}} \cdot \delta \mathbf{a}_3 &= +2\pi/3, \end{aligned} \quad (25)$$

we obtain the result

$$w'_1 = -\frac{t_{\perp}^{(1)}}{l} \left[1 + 6 \operatorname{Re} \sum_{n_1=1}^n \sum_{n_2=0}^{n_1-1} (e^{i2\pi/3})^{n_1+n_2} \right]. \quad (26)$$

for (23) at $+K_{\bar{M}}\hat{\mathbf{x}}$ in the simple case where $t_{\perp}^{(1)}$ is a constant over the Wigner-Seitz unit cell. Above, in (25), we have used the result $\sqrt{l}(2 \sin \alpha) = 1$ at $m = n + 1$, by (1) and (2). Because the A-B twist centers show 6-fold rotation symmetry, which includes inversion symmetry (see Fig. 1), the matrix element w'_1 is necessarily real. Importantly, notice that the oscillatory exponential factor above in general will result in a small matrix element of order $t_{\perp}^{(1)}/l$. A direct summation of the geometric series (26) yields the particular result $w'_1 = 2(t_{\perp}^{(1)}/l)[\cos 2\pi(n-1)/3]$. (See Appendix C.) The small

inter-valley matrix element w'_1 is consistent with the Bistritzer-MacDonald method[7], in which case w'_1 is neglected.

Next, we shall compute the inter-graphene-sheet matrix element w'_0 of the truncated hamiltonian (20). It is given by the expression

$$\langle\langle \mathbf{k}_i, A, - | H | \mathbf{k}_i, A, + \rangle\rangle = - \sum_{\delta \mathbf{r}_{A/A}} \frac{t_{\perp}^{(0)}}{l} e^{-i \mathbf{k}_i \cdot [\delta \mathbf{r}_{A/A}(-) - \delta \mathbf{r}_{A/A}(+)]} \quad (27)$$

for inter-graphene-sheet matrix elements (18) at momenta $\mathbf{k}_i = \mathbf{k} - \mathbf{G}$ near $K_{\bar{M}}\hat{\mathbf{x}}$. The displacements of the links in between the sheets of graphene from the center of the Wigner-Seitz unit cell are given by $\delta \mathbf{r}_{A/A}(\pm) = m_1 \mathbf{c}_1(\pm) + m_2 \mathbf{c}_2(\pm)$, where m_1 and m_2 are integers that satisfy the condition $m_1 + m_2 \bmod 3 = 1$. Figure 3 displays that A-A links show 3-fold rotation symmetry. This results in a null matrix element (27) as we will now demonstrate. Each group of three terms in the matrix element (27) related by 120° rotations is proportional to $\zeta_{A/A}^{(m_1, m_2)}(K_{\bar{M}}\hat{\mathbf{x}})$, where

$$\zeta_{A/A}^{(m_1, m_2)}(\mathbf{k}) = e^{i \mathbf{k} \cdot \delta \mathbf{c}_0(m_1, m_2)} + e^{i \mathbf{k} \cdot \delta \mathbf{c}_+(m_1, m_2)} + e^{i \mathbf{k} \cdot \delta \mathbf{c}_-(m_1, m_2)}, \quad (28)$$

with

$$\begin{aligned} \delta \mathbf{c}_0(m_1, m_2) &= m_1 \delta \mathbf{c}_1 + m_2 \delta \mathbf{c}_2, \\ \delta \mathbf{c}_+(m_1, m_2) &= m_1 \delta \mathbf{c}_2 + m_2 \delta \mathbf{c}_3, \\ \delta \mathbf{c}_-(m_1, m_2) &= m_1 \delta \mathbf{c}_3 + m_2 \delta \mathbf{c}_1, \end{aligned} \quad (29)$$

and where

$$\begin{aligned} \delta \mathbf{c}_1 &= \mathbf{c}_1(+) - \mathbf{c}_1(-) = a(2 \sin \alpha) \hat{\mathbf{y}}, \\ \delta \mathbf{c}_2 &= \mathbf{c}_2(+) - \mathbf{c}_2(-) = a(2 \sin \alpha) \left(-\frac{\sqrt{3}}{2} \hat{\mathbf{x}} - \frac{1}{2} \hat{\mathbf{y}} \right), \\ \delta \mathbf{c}_3 &= \mathbf{c}_3(+) - \mathbf{c}_3(-) = a(2 \sin \alpha) \left(\frac{\sqrt{3}}{2} \hat{\mathbf{x}} - \frac{1}{2} \hat{\mathbf{y}} \right). \end{aligned} \quad (30)$$

Using the following results for the dot products at $m - n = 1$,

$$\begin{aligned} K_{\bar{M}}\hat{\mathbf{x}} \cdot \delta \mathbf{c}_1 &= 0, \\ K_{\bar{M}}\hat{\mathbf{x}} \cdot \delta \mathbf{c}_2 &= -2\pi/3, \\ K_{\bar{M}}\hat{\mathbf{x}} \cdot \delta \mathbf{c}_3 &= +2\pi/3, \end{aligned} \quad (31)$$

direct calculation then yields

$$\begin{aligned} \zeta_{A/A}^{(m_1, m_2)}(K_{\bar{M}}\hat{\mathbf{x}}) &= (e^{i2\pi/3})^{m_1} + (e^{i2\pi/3})^{m_2-m_1} + (e^{i2\pi/3})^{-m_2} \\ &= (e^{i2\pi/3})^{m_2-m_1} [(e^{i2\pi/3})^{2m_1-m_2} + 1 + (e^{i2\pi/3})^{m_1-2m_2}] \\ &= (e^{i2\pi/3})^{m_2-m_1} [(e^{i2\pi/3})^{-(m_1+m_2)} + 1 + (e^{i2\pi/3})^{(m_1+m_2)}]. \end{aligned} \quad (32)$$

It is equal to zero in the present case, where $(m_1 + m_2) \bmod 3 = 1$. Similar three-fold rotation-symmetric calculation yields that the first non-trivial order of this matrix

Out[]:=

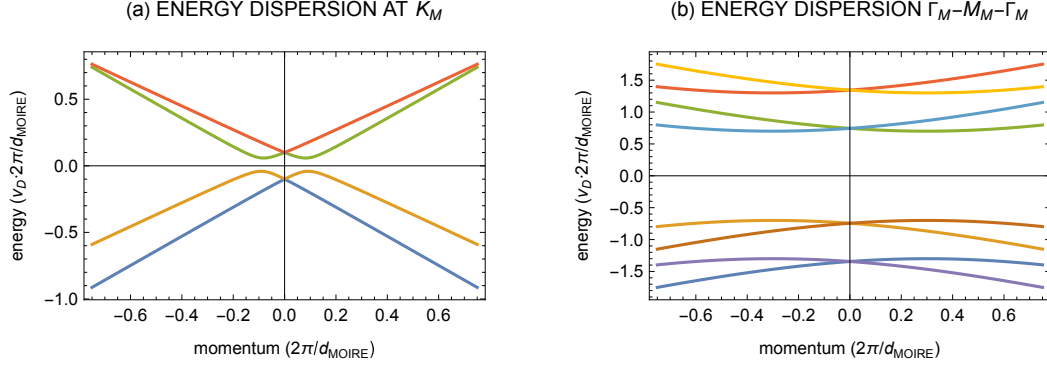


Figure 7. (a) Dispersion about momentum K_M of low-energy bands as predicted by degenerate perturbation theory, (33) and (35). Here, we have set $\sin(\alpha - \delta) = \sqrt{3}/2$, and $w_0^{(1)} = -0.1 v_D$ and $w_1' = -0.1 v_D \cdot 2\pi/d_{\text{moire}}$, with $d_{\text{moire}} = \sqrt{l}d$, where $d = \frac{\sqrt{3}}{2}a_{\Delta}$. (b) Dispersion along $\Gamma_M - M_M - \Gamma_M$ of low-energy bands as predicted by degenerate perturbation theory, (33) and (45). Here, we have set $w_0^{(0)} = -0.3 v_D \cdot 2\pi/d_{\text{moire}} = w_1$.

element with $\delta\mathbf{k}$ has the form $w_0' \cong w_0^{(1)}(\delta k_x - i\delta k_y)$. In the simple case where $t_{\perp}^{(0)}$ is constant over the Wigner-Seitz unit cell, direct summation of the resulting geometric series at $m - n = 1$ yields $\lim_{n \rightarrow \infty} w_0^{(1)} = -(a t_{\perp}^{(0)}/l) \sin[2\pi(n-1)/3]$. (See Appendix C.) Notice, importantly, that this group velocity of the matrix element is small, and of order $at_{\perp}^{(0)}/l$, or zero. It is also thereby consistent with the Bistritzer-MacDonald method[7], which neglects such transitions.

We shall now show that inter-valley mixing results in a small band gap for twisted bi-layer graphene at commensurate twist angles along the Periodic Moiré Pattern line. The characteristic equation associated with the truncated 4×4 hamiltonian (20) is

$$0 = \varepsilon^4 + a_2\varepsilon^2 + a_1\varepsilon + a_0, \quad (33)$$

with coefficients

$$\begin{aligned} a_2 &= -2(|w_0'|^2 + w_1'^2 + |z|^2), \\ a_1 &= -2[w_0'(z_+ + z_-) + w_0'^*(z_+^* + z_-^*)]w_1', \\ a_0 &= (w_1'^2 - |w_0'|^2)^2 - w_1'^2(z_+z_-^* + z_+^*z_-) \\ &\quad - w_0'^2z_+z_- - w_0'^{*2}z_+^*z_-^* + |z|^4. \end{aligned} \quad (34)$$

Above, w_1' is assumed to be real, and $|z_+| = |z| = |z_-|$. Plugging in expressions (22) and $w_0' = w_0^{(1)}(\delta k_x - i\delta k_y)$ yields the following expressions for the above coefficients:

$$\begin{aligned} a_2 &= -2[w_1'^2 + (v_D^2 + w_0^{(1)2})|\delta\mathbf{k}|^2], \\ a_1 &= 8[\sin(\alpha - \delta)]w_1'w_0^{(1)}v_D|\delta\mathbf{k}|^2, \\ a_0 &= w_1'^4 + 2w_1'^2\{\cos 2(\alpha - \delta)v_D^2 - w_0^{(1)2}\}|\delta\mathbf{k}|^2 + (v_D^2 - w_0^{(1)2})^2|\delta\mathbf{k}|^4. \end{aligned} \quad (35)$$

At $|w_0^{(1)}| \ll v_D$, the first-order term $a_1\varepsilon$ in (33) can be neglected at large enough momentum $|\delta\mathbf{k}|$. This yields the dispersions in energy:

$$\varepsilon_{\pm}^{(0)2} = (v_D|\delta\mathbf{k}| \pm [\sin(\alpha - \delta)]w_1')^2 + ([\cos(\alpha - \delta)]w_1')^2. \quad (36)$$

Out[]:=

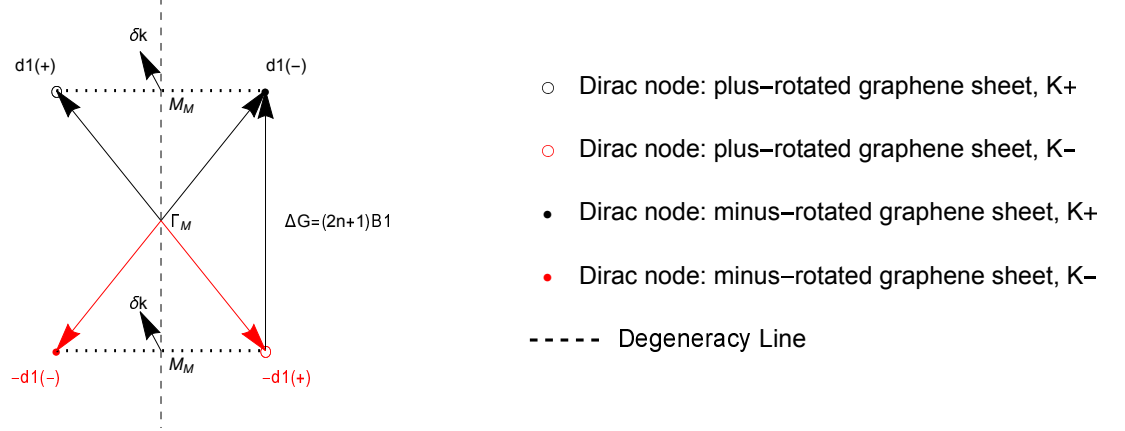


Figure 8. Schematic depiction of “twisted” Dirac nodes following Bistritzer and MacDonald ref. [7]. They are bisected by the (degeneracy) line M_M - Γ_M - M_M in momentum space.

It reveals that such twisted bi-layer graphene is an insulator at charge neutrality, with a small gap in the energy bands: $2\Delta_0 = 2|\cos(\alpha - \delta)]w'_1|$. Notice that the above approximation for the low-energy spectrum (36) shows particle-hole symmetry. This is an artifact. Treating the former first-order term in the characteristic equation (33) as a perturbation results in a first-order correction (49) to $\varepsilon_{\pm}^{(0)}$ that breaks particle-hole symmetry. Figure 7 (a) shows the energy dispersion around K_M that is predicted by degenerate perturbation theory upon a numerical solution of (33) and (35). As expected, particle-hole symmetry is broken.

Last, what is the nature of inter-valley mixing at the opposing point in momentum, $K_{\bar{M}}\hat{\mathbf{x}} \rightarrow -K_{\bar{M}}\hat{\mathbf{x}}$? It can easily be shown that the graphene matrix elements in the corresponding truncated 4×4 hamiltonian (22) are negative complex conjugates of each other: $z_{\pm} \rightarrow -z_{\pm}^*$. Furthermore, the inter-graphene sheet matrix elements (18) are given by $w_0^*(-\mathbf{k})$ and $w_1^*(-\mathbf{k})$. Hence, we have the replacements in w'_0 : $\delta k_x + i\delta k_y \rightarrow \delta k_x - i\delta k_y$ and $w_0'^{(1)} \rightarrow -w_0'^{(1)}$. The corresponding A/B inter-sheet matrix element w'_1 is a non-zero real number at $K_{\bar{M}}\hat{\mathbf{x}}$, and it therefore remains unchanged. Inspection of the characteristic equation (33) and (34) plus the above replacements yields that the energy eigenvalues remain unchanged: $\varepsilon \rightarrow \varepsilon$.

4.2. Electron Energy Spectrum near Middle of Edge Moiré Brillouin Zone

We shall now reveal the origin of the band-flattening effect in twisted bi-layer graphene by analyzing the hopping hamiltonian at momenta in the vicinity of M_M within degenerate perturbation theory. We shall, in particular, follow the idea proposed by Bistritzer and MacDonald [7] of “twisting” the Dirac nodes. The black arrows in Fig. 6 correspond to these (8): $\mathbf{d}_1(+)$ and $\mathbf{d}_1(-)$. Because the k_y momentum axis bisects the latter two Dirac nodes, any momentum point on that axis has corresponding graphene energy eigenvalues that are degenerate. Here, the origin in momentum space is defined

by the twist center of the momentum arrows in Fig. 6. The same is true of the pair of Dirac nodes at $-\mathbf{d}_1(+)$ and $-\mathbf{d}_1(-)$, which are the red arrows in Fig. 6. Figure 8 summarizes the previous. Below, we will work out the degenerate perturbation theory of these two pairs of Dirac nodes.

We will now apply degenerate perturbation theory in the limit of weak hopping in between the sheets of graphene, at momenta $\mathbf{k} - \mathbf{G}$ near the point $+M_M\hat{\mathbf{y}}$ that bisects the “twisted” Dirac nodes located at $\mathbf{d}_1(+)$ and $\mathbf{d}_1(-)$. Here, $M_M = (\cos \alpha)K$. This approximation is described by the truncated 4×4 hamiltonian of the form

$$H_{M_M+}(\delta\mathbf{k}) = \begin{bmatrix} 0 & z_- & w_0 & w_1 \\ z_-^* & 0 & w_1 & w_0^* \\ w_0^* & w_1^* & 0 & z_+ \\ w_1^* & w_0 & z_+^* & 0 \end{bmatrix}. \quad (37)$$

Here, we express the momentum as $\mathbf{k} - \mathbf{G} = M_M\hat{\mathbf{y}} + \delta\mathbf{k}$. Above, we have intra-graphene matrix elements $z_{\pm} = -t_{\parallel}\zeta_{\pm}(\mathbf{k} - \mathbf{G})$ at momenta $\mathbf{k} - \mathbf{G}$ in the vicinity of $M_M\hat{\mathbf{y}}$. As in the previous case, we approximate $\zeta_{\pm}(\mathbf{k} - \mathbf{G}) = e^{i\mathbf{d}_1(\pm)\cdot\mathbf{c}_1(\pm)}\zeta'_{\pm}(\mathbf{d}_1(\pm) + \delta\mathbf{k})$ at the Dirac nodes. Notice, first, that the phase factor is unity because $\mathbf{d}_1(\pm)$ and $\mathbf{c}_1(\pm)$ are perpendicular. Also, $\zeta'_{\pm}(\mathbf{k} - \mathbf{G})$ is periodic over the \pm -rotated reciprocal lattice by (21). We therefore have the intra-graphene matrix elements

$$\begin{aligned} z_- &= -v_D e^{i\alpha} i(k_{-,x} + ik_{-,y}), \\ z_+ &= -v_D e^{-i\alpha} i(k_{+,x} + ik_{+,y}). \end{aligned} \quad (38)$$

Above, $\mathbf{k}_{\pm} = \mathbf{k} - \mathbf{G} - \mathbf{d}_1(\pm)$.

We shall next compute the inter-graphene A-B matrix element w_1 in the truncated 4×4 hamiltonian (37). This is achieved by repeating the previous calculation of w'_1 at momentum $K_{\bar{M}}\hat{\mathbf{x}}$ (23)-(25), but instead at momentum $M_M\hat{\mathbf{y}}$. The relevant dot products in this case are:

$$\begin{aligned} M_M\hat{\mathbf{y}} \cdot \delta\mathbf{a}_1 &= 0, \\ M_M\hat{\mathbf{y}} \cdot \delta\mathbf{a}_2 &= -(2\pi/3)\sqrt{3}(\sin \theta), \\ M_M\hat{\mathbf{y}} \cdot \delta\mathbf{a}_3 &= +(2\pi/3)\sqrt{3}(\sin \theta). \end{aligned} \quad (39)$$

After applying 3-fold rotation symmetry to the sum over hopping links in between sheets of graphene (23), we obtain the result

$$w_1 = -\frac{t_{\perp}^{(1)}}{l} \left[1 + 2 \operatorname{Re} \sum_{n_1=1}^n \sum_{n_2=0}^{n_1-1} (z_0^{-n_2} + z_0^{n_2-n_1} + z_0^{n_1}) \right] \quad (40)$$

in the simple case that $t_{\perp}^{(1)}$ is uniform, where $z_0 = \exp[i(2\pi/3)\sqrt{3}(\sin \theta)]$. Again, A-B twist centers also show space-inversion symmetry, which implies that w_1 must be real. Along the Periodic Moiré Pattern line, $m = n + 1$, it is easily shown from (1) that $\lim_{n \rightarrow \infty} z_0 = \exp\{i2\pi/[3(n + \frac{1}{2})]\}$. Direct evaluation of the geometric series sums (40) in this limit yields the result

$$\lim_{n \rightarrow \infty} w_1 = -\frac{3}{2\pi} \left(\frac{1}{\sqrt{3}} + \frac{3}{2\pi} \right) t_{\perp}^{(1)} \cong -0.5036 t_{\perp}^{(1)}. \quad (41)$$

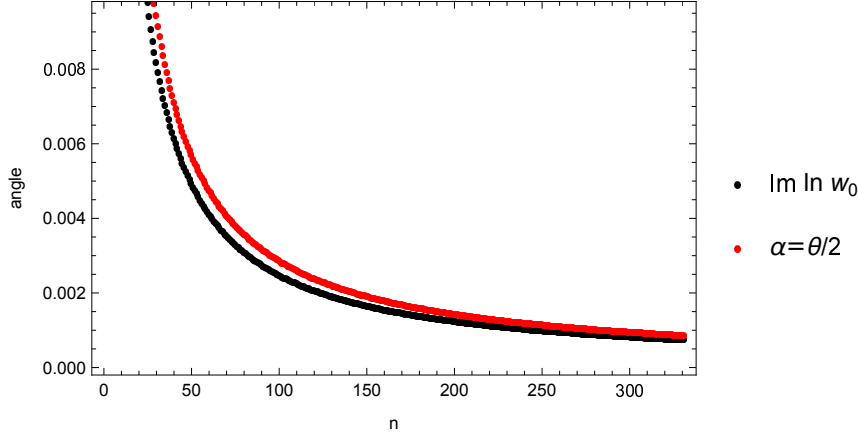


Figure 9. Comparison of $\text{Im} \ln w_0$ and half the twist angle, α , versus n along the Periodic Moiré Pattern line, $m = n + 1$. The nearest-neighbor hopping matrix elements $t_{\perp}^{(0)}$ between the two graphene sheets are uniform. See Appendix C.3 for closed form expressions of w_0 .

This is shown in Appendix C.3 from closed-form expressions of the geometric series sums (40).

Next, we shall compute the matrix element between A sites of different sheets of graphene, w_0 , in the truncated 4×4 hamiltonian (37). As in the previous subsection, it is given by the expression (27), but evaluated at momenta $\mathbf{k}_i = \mathbf{k} - \mathbf{G}$ near $M_M \hat{\mathbf{y}}$ instead. Recall that $M_M = (\cos \alpha)K$. Again, it is useful to compute the matrix element in a 3-fold symmetric way, as described by expressions (28)-(30), where m_1 and m_2 are integers that satisfy the condition $(m_1 + m_2) \bmod 3 = 1$. Using the following results for the dot products,

$$\begin{aligned} M_M \hat{\mathbf{y}} \cdot \delta \mathbf{c}_1 &= \frac{4\pi \sin \theta}{3 \sqrt{3}}, \\ M_M \hat{\mathbf{y}} \cdot \delta \mathbf{c}_2 &= -\frac{2\pi \sin \theta}{3 \sqrt{3}}, \\ M_M \hat{\mathbf{y}} \cdot \delta \mathbf{c}_3 &= -\frac{2\pi \sin \theta}{3 \sqrt{3}}, \end{aligned} \quad (42)$$

direct calculation then yields

$$\zeta_{A/A}^{(m_1, m_2)}(M_M \hat{\mathbf{y}}) = (z_0^{1/3})^{2m_1 - m_2} + (z_0^{1/3})^{-m_1 - m_2} + (z_0^{1/3})^{2m_2 - m_1}. \quad (43)$$

In the simple case where $t_{\perp}^{(0)}$ is uniform over the Wigner-Seitz unit cell, numerical evaluation of the resulting closed-form expressions for the geometric series sums yields the form $w_0 = w_0^{(0)} e^{i\alpha}$ for the matrix element at momentum $+M_M \hat{\mathbf{y}}$, where $w_0^{(0)}$ is real at large integer parameter n . This is demonstrated by Fig. 9. It is also true that the limit $\lim_{n \rightarrow \infty} w_0$ at momentum $+M_M \hat{\mathbf{y}}$ coincides with the corresponding limit (41) for w_1 , but with the replacement $t_{\perp}^{(1)} \rightarrow t_{\perp}^{(0)}$. The above results are based on summations of geometric series in closed form that emerge from the summation of (43) over the A-A links shown by Fig. 3. Those calculations are carried out in Appendix C.3.

We shall now show how energy-level repulsion at the point M_M on the edge of the first moiré Brillouin zone can result in flat energy bands near zero energy. The characteristic equation associated with the truncated 4×4 hamiltonian (37) again has the fourth-order polynomial form (33), but with coefficients

$$\begin{aligned} a_2 &= -2[|w_0|^2 + w_1^2 + (|z_-|^2 + |z_+|^2)/2], \\ a_1 &= -2[w_0(z_+ + z_-^*) + w_0^*(z_+^* + z_-)]w_1, \\ a_0 &= (w_1^2 - |w_0|^2)^2 - w_1^2(z_+z_- + z_+^*z_-^*) \\ &\quad - w_0^2z_+z_-^* - w_0^{*2}z_+^*z_- + |z_+|^2|z_-|^2. \end{aligned} \quad (44)$$

Above, w_1 is assumed to be real. The wavenumbers in the forms (38) for the intra-graphene matrix elements z_+ and z_- follow $k_{+,x} = +k_x$, $k_{-,x} = -k_x$, $k_{+,y} = \delta k_y = k_{-,y}$ along the y axis that bisects the two Dirac nodes at $\mathbf{d}_1(+)$ and $\mathbf{d}_1(-)$. (See Fig. 6.) Here, k_x is the displacement of the $-$ Dirac node from the bisecting y axis. (See Fig. 8.) Substitution into (44) yields the corresponding coefficients for the characteristic equation (33):

$$\begin{aligned} a_2 &= -2[w_0^{(0)2} + w_1^2 + v_D^2k_x^2 + v_D^2(\delta k_y)^2], \\ a_1 &= -8w_0^{(0)}w_1v_D(\delta k_y), \\ a_0 &= (w_1^2 - w_0^{(0)2})^2 - 2(w_1^2 - w_0^{(0)2})v_D^2k_x^2 \\ &\quad - 2(w_1^2 + w_0^{(0)2})v_D^2(\delta k_y)^2 + v_D^4[k_x^2 + (\delta k_y)^2]^2. \end{aligned} \quad (45)$$

At the point M_M in momentum space, we have $\delta k_y = 0$. This yields the coefficients $a_1 = 0$ and $a_0 = [w_1^2 - w_0^{(0)2} - (v_Dk_x)^2]^2$. The energy eigenvalues are then easily obtained, and they are given by

$$\varepsilon_{\pm}^{(0)2}(M_M) = -\frac{a_2}{2} \pm \sqrt{\left(\frac{a_2}{2}\right)^2 - a_0}. \quad (46)$$

Above, $\varepsilon_-^{(0)}(M_M)$ and $\varepsilon_+^{(0)}(M_M)$ are closer and farther away from zero energy, respectively. Because $a_1 = 0$, the condition $\varepsilon_-(M_M) = 0$ suggests that a flattest energy band occurs at $a_0 = 0$. Hence, by the previous result for a_0 at $\delta k_y = 0$, degenerate perturbation theory at M_M predicts a flat energy band when

$$v_Dk_x = \sqrt{w_1^2 - w_0^{(0)2}}. \quad (47)$$

The magic twist angle is thereby obtained from the relation $k_x = K(\sin \alpha)$. It yields the formula

$$2 \sin \alpha_* = \sqrt{w_1^2 - w_0^{(0)2}}/(v_DK/2) \quad (48)$$

for the magic twist angle.

And what is the dispersion of the energy bands closest to zero energy along the bisecting y axis? Inspection of the coefficients (45) yields that a_1 is linear order in δk_y , while the remaining coefficients are quadratic in it. The characteristic equation (33) can

be solved to first order in a_1 (δk_y): $\varepsilon = \varepsilon^{(0)} + \varepsilon^{(1)}$. This yields the following expression for the first-order correction:

$$\varepsilon_{\pm}^{(1)} = -\frac{a_1}{2(2\varepsilon_{\pm}^{(0)2} + a_2)}. \quad (49)$$

Substituting in the result (46) for $\varepsilon_{\pm}^{(0)2}$ yields the result for the first-order correction:

$$\varepsilon_{\pm}^{(1)} = \mp \frac{a_1}{2\sqrt{a_2^2 - 4a_0}}. \quad (50)$$

In turn, to lowest order in δk_y , substituting in the coefficients (45) a_n of the characteristic equation above yields the final result:

$$\varepsilon_{\pm}^{(1)} = \pm v_D(\delta k_y). \quad (51)$$

The dispersion of the energy along the bisecting y axis is then linear in k_y near the high-symmetry point M_M .

And as predicted by degenerate perturbation theory, what is the nature of the energy spectrum near the opposing point in momentum, $-M_M\hat{\mathbf{y}}$, which bisects the pair of Dirac nodes at $-\mathbf{d}_1(-)$ and $-\mathbf{d}_1(+)$? These are depicted in Fig. 8 by the red arrows. The truncated hamiltonian is once again a 4×4 matrix of the form (37), but with z_- and z_+ replaced by

$$\begin{aligned} \bar{z}_- &= -v_D e^{-i\alpha} i(k_{+,x} - ik_{+,y}), \\ \bar{z}_+ &= -v_D e^{i\alpha} i(k_{-,x} - ik_{-,y}), \end{aligned} \quad (52)$$

and with w_0 replaced by w_0^* . The matrix element w_1 is real, and it therefore remains unchanged. Inspection of the characteristic equation (33) and (45) then yields that the energy eigenvalues are replaced by $\varepsilon \rightarrow -\varepsilon$. This implies that the energy spectrum near zero energy and momentum M_M shows particle-hole symmetry. Furthermore, the first-order correction in δk_y to the energy is minus that due to the opposite valley (51). This implies that the dispersion of the lowest-energy bands *cross* at the high-symmetry point M_M as a function of momentum along the bisecting y axis.

We can now answer the following question. What is the energy dispersion as δk_y gets farther away from the high-symmetry point M_M ? Consider $w_0^{(0)}$ as a perturbation instead of δk_y . It is straight-forward to show that the energy eigenvalues (46) at $w_0^{(0)} = 0$ are plus or minus $|\varepsilon_{\pm}^{(0)}| = v_D \sqrt{k_x^2 + (\delta k_y)^2} \pm w_1$. As expected, the degenerate energy from the Dirac cones is split by hopping in between the graphene sheets. Further calculation yields the perturbation (49) $\varepsilon_{\pm}^{(1)} = \pm w_0^{(0)} [(\delta k_y)/\sqrt{k_x^2 + (\delta k_y)^2}]$. To second order in δk_y , this yields approximate energy dispersions near the M_M+ point in momentum space:

$$\begin{aligned} \varepsilon_{\pm, >} &\cong +v_D k_x \pm w_1 - \frac{1}{2} \frac{w_0^{(0)2}}{v_D k_x} + \frac{1}{2} \frac{1}{v_D k_x} [v_D(\delta k_y) \pm w_0^{(0)}]^2, \\ \varepsilon_{\pm, <} &\cong -v_D k_x \mp w_1 + \frac{1}{2} \frac{w_0^{(0)2}}{v_D k_x} - \frac{1}{2} \frac{1}{v_D k_x} [v_D(\delta k_y) \mp w_0^{(0)}]^2. \end{aligned} \quad (53)$$

n	m	l	θ	$v_D K_M/2 = (\pi/\sqrt{3l})t_{\parallel}$
29	30	2611	1.121°	$0.0355 t_{\parallel}$
30	31	2791	1.085°	$0.0343 t_{\parallel}$
31	32	2977	1.050°	$0.0332 t_{\parallel}$

Table 1. Integer parameters for bi-layer graphene at commensurate twist angles θ along the Periodic Moiré Pattern line that are near the experimental magic twist angle. The last column is the prediction by zone-folding of the energy at the M_M point of the first positive-energy band.

Likewise, the M_M – point in momentum space yields minus the above dispersions:

$$\begin{aligned}
-\varepsilon_{\pm,>} &\cong -v_D k_x \mp w_1 + \frac{1}{2} \frac{w_0^{(0)2}}{v_D k_x} - \frac{1}{2} \frac{1}{v_D k_x} [v_D (\delta k_y) \pm w_0^{(0)}]^2, \\
-\varepsilon_{\pm,<} &\cong +v_D k_x \pm w_1 - \frac{1}{2} \frac{w_0^{(0)2}}{v_D k_x} + \frac{1}{2} \frac{1}{v_D k_x} [v_D (\delta k_y) \mp w_0^{(0)}]^2.
\end{aligned} \tag{54}$$

Above, $\varepsilon_{\pm,>}$ in (53) and $-\varepsilon_{\pm,<}$ in (54) are both positive, and they “cross” at M_M , while $\varepsilon_{\pm,<}$ in (53) and $-\varepsilon_{\pm,>}$ in (54) are both negative, and they also “cross” at M_M . Notice that the “cross” dispersion at M_M eventually turns away from zero energy as δk_y gets large enough. This is confirmed by Fig. 7 (b), where the roots of the characteristic equation, (33) and (45), are obtained numerically.

5. Numerical Calculation of the Electron Energy Spectrum

Below, we find the energy eigenvalues of the nearest-neighbor electron hopping model for twisted bi-layer graphene that was introduced in subsection 3.2. Commensurate twist angles near 1.1° shall be studied. (See Table 1.) Four flat bands near zero energy emerge at “magic” values of the matrix elements for hopping in between the twisted sheets of graphene.

5.1. Hamiltonian Matrix

The nearest neighbor electron hopping hamiltonian for bi-layer graphene at commensurate twist angles was constructed in section 3.2 in momentum space. It has the form (19), with intra-graphene matrix elements H_{--} and H_{++} given by (13) and (14), and with inter-graphene matrix elements H_{-+} and H_{+-} given by (18) and the hermitian conjugate. The 3-fold rotation symmetry of twisted bi-layer graphene shown by Fig. 1, for example, can be exploited to compute the latter. Such calculations are described in Appendix C.1. Last, a gauge transformation that moves the phase factors from the inter-graphene-sheet A-B matrix elements (18) to the A-A(B-B) ones is made. It is described in Appendix A.

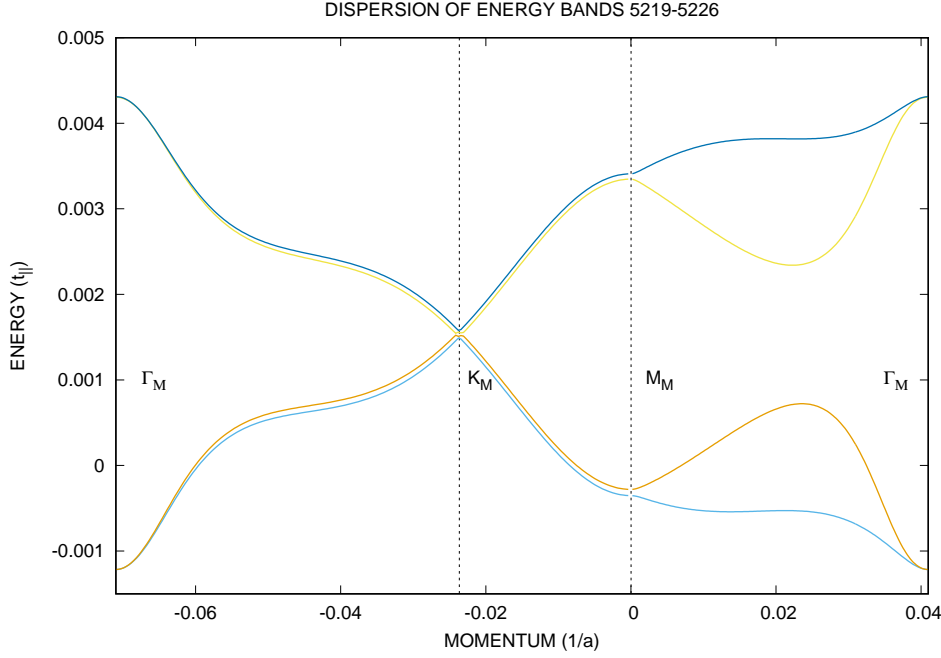


Figure 10. Dispersion of flat energy bands near zero energy for hopping hamiltonian in momentum space (19) of dimensions $4l \times 4l$, with $l = 2611$ A(B) sites per sheet of graphene inside a moiré unit cell. (See Table 1.) Inter-graphene-sheet matrix elements are uniform over nearest neighbors, and they are set to $t_{\perp}^{(1)} = 0.069 t_{\parallel} = t_{\perp}^{(0)}$.

The dimensions of the hopping hamiltonian matrix are $4l \times 4l$, where l is the number of A (B) sites inside of a true moiré unit cell per sheet of graphene (2). Energy eigenvalues of the hamiltonian matrix are obtained by using standard numerical routines for dense matrices. We shall restrict the numerical calculations to commensurate lattices along the Periodic Moiré Pattern line, $m = n + 1$, that are closest to the experimental magic twist angle of $\theta = 1.1^\circ$. These are listed in Table 1. They result in the smallest possible dimensions for the hopping hamiltonian matrix.

5.2. Ideal Nearest Neighbor Hopping Between Twisted Sheets of Graphene

Figure 10 shows the flat bands of the energy spectrum near the magic twist angle for integer parameters $n = 29$, $m = 30$, and $l = 2611$. The hopping matrix elements in between graphene sheets are set to $t_{\perp}^{(1)} = 0.069 t_{\parallel} = t_{\perp}^{(0)}$ across all nearest neighbor links. These are depicted, respectively, by Figs. 2 and 3. By comparison, the bandwidth of these flat bands reaches a minimum at inter-graphene-sheet matrix elements $t_{\perp}^{(1)} = 0.072 t_{\parallel} = t_{\perp}^{(0)}$. Notice that the difference in energy between the M_M point and the K_M point in Fig. 10 is an order of magnitude smaller than that predicted by zone folding in Table 1. The level crossing along Γ_M - M_M - Γ_M at the M_M point that is predicted by degenerate perturbation theory, Fig. 7 b, is evident. There is a small amount of level repulsion there too, however. It is a result of inter-valley mixing. And as predicted by degenerate perturbation theory, Fig. 7 a, the results of inter-valley mixing

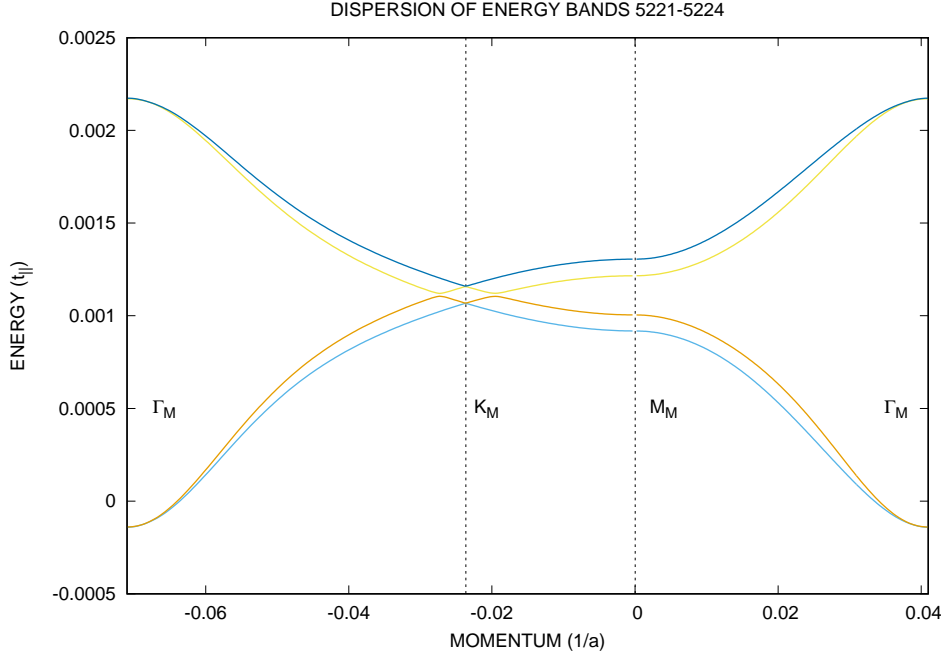


Figure 11. Flat energy bands near zero energy for hopping hamiltonian (19), with $l = 2611$ A(B) sites per sheet of graphene inside a moiré unit cell. (See Table 1.) “Relaxed” hopping matrix elements are uniform over nearest neighbors between the graphene sheets, and they are set to $t_{\perp}^{(1)} = 0.079 t_{\parallel}$ and to $t_{\perp}^{(0)} = 0.0395 t_{\parallel}$.

are also visible at the K_M point. Last, the remaining two cases of commensurate magic twist angles listed in Table 1 give similar results for the flat energy bands at $t_{\perp}^{(0)} = t_{\perp}^{(1)}$.

5.3. “Relaxed” Nearest Neighbor Hopping Between Twisted Sheets of Graphene

The bi-layer graphene crystals at commensurate twist angles considered in this paper have honeycomb moiré unit cells with Bernal stacks at the vertices. Figure 1 displays this in the case of the smallest commensurate twisted bi-layer graphene crystal, with integer parameters $m = 2$, $n = 1$, and $l = 7$. In addition, the center of such honeycomb moiré unit cells coincides with a twist center for A-A links in between the two sheets of graphene. Given the small twist angle of 1.1° that is experimentally observed in twisted bi-layer graphene, A(B) sites in between the two sheets of graphene will lie practically right above/below each other in the vicinity of such twist centers. It has been pointed out that strain will develop in this region of the moiré unit cell in the ideal twisted bi-layer graphene crystal so that nearest neighbor links of A(B) sites in between the two sheets of graphene become more separated in the intra-graphene directions[11][12][13][14][15][16]. Below, we shall model this effect by assuming uniform hopping between nearest neighbor A(B) sites in between graphene sheets, $t_{\perp}^{(0)}$, and by assuming uniform hopping between nearest neighbor A sites in one sheet of graphene with a B site in the other sheet of graphene, $t_{\perp}^{(1)}$, but while satisfying the inequality $t_{\perp}^{(0)} < t_{\perp}^{(1)}$. By the previous, the ratio $t_{\perp}^{(0)}/t_{\perp}^{(1)}$ coincides with the ratio of matrix elements at the M_M point in momentum space,

$w_{A-,A+}/w_{A-,B+}$. It coincides with the reduction factor for the A-A(B-B) links versus the A-B links in the moire patterns of twisted bi-layer graphene[17].

Figure 11 shows the “relaxed” flat bands of the energy spectrum near the magic twist angle for integer parameters $n = 29$, $m = 30$, and $l = 2611$. The hopping matrix elements in between graphene sheets are set to $t_{\perp}^{(1)} = 0.079 t_{\parallel}$ and to $t_{\perp}^{(0)} = 0.0395 t_{\parallel}$, which is half of the former, across all nearest neighbor links. This choice of inter-graphene-sheet hopping matrix elements therefore lies halfway between the previous ideal case and the chiral limit, $t_{\perp}^{(0)} = 0$, in which case the central bands are perfectly flat[10]. Figures 2 and 3 depict these inter-graphene-sheet links, respectively. By comparison, the bandwidth of these “relaxed” flat bands reaches a minimum at inter-graphene-sheet matrix elements $t_{\perp}^{(1)} = 0.078 t_{\parallel}$ and $t_{\perp}^{(0)} = 0.039 t_{\parallel}$, which again is half the former. Figure 11 shows that the splitting of valley degeneracy exists in general at all momenta. Also, the difference between the energy at the M_M point and the energy at the K_M is two orders of magnitude smaller than that predicted by zone-folding in Table 1. Again, the remaining two cases of commensurate magic twist angles listed in Table 1 give similar results for the flat energy bands at $t_{\perp}^{(0)} = t_{\perp}^{(1)}/2$.

5.4. Magic Twist Angle versus Degenerate Perturbation Theory

By formula (47), degenerate perturbation theory predicts that flat electron bands emerge when the energy at M_M predicted by zone folding in the first positive-energy band is equal to $\sqrt{w_1^2 - w_0^2}$. In the limit of large integer parameters along the Periodic Moiré Pattern line, $m = n + 1$, degenerate perturbation theory also predicts that $w_1 = -0.5 t_{\perp}^{(1)}$ and $w_0 = -0.5 t_{\perp}^{(0)}$. Recall that the “relaxed” flat bands depicted by Fig. 11 occur near an optimally flat point at $t_{\perp}^{(1)} = 0.078 t_{\parallel}$ and $t_{\perp}^{(0)} = t_{\perp}^{(1)}/2$. Hence, by the previous, $\sqrt{w_1^2 - w_0^2} = (\sqrt{3}/2)w_1 = 0.0338 t_{\parallel}$. This calculation compares well with the result from zone-folding, $v_D K_M/2 = 0.0355 t_{\parallel}$, that is listed in Table 1 at the corresponding twist angle, which is what is predicted by degenerate perturbation theory (47).

Figure 10, on the other hand, shows flat bands at ideal inter-graphene-sheet hopping. It lies near an optimally flat point at $t_{\perp}^{(1)} = 0.072 t_{\parallel} = t_{\perp}^{(0)}$. In the ideal case, however, we generally have that $\sqrt{w_1^2 - w_0^2} \cong 0$ at large integer parameter n . It thereby compares badly with the answer from zone-folding that is listed in Table 1, which is what is predicted by degenerate perturbation theory (47).

6. Discussion

Below, we compare the bi-layer graphene lattice at commensurate twist angles studied here to the Bistritzer-MacDonald twist construction of the reciprocal lattice[7]. We also reveal the connection between inter-valley mixing (26) and spiral Kekulé order.

6.1. Moiré Patterns with Subcells in Twisted Bi-Layer Graphene

The bi-layer graphene lattices studied above in section 2 have commensurate twist angles characterized by relatively prime integer parameters [8][9] $m > n$, where half the twist angle α is given by (1) and (2). It is instructive to compute the difference between Dirac nodes in the minus-rotated sheet of graphene and the plus-rotated sheet of graphene:

$$\mathbf{d}_1(-) - \mathbf{d}_1(+) = (m - n)\mathbf{D}_1 \quad (55)$$

by (8). At $m = n + 1$, the twist in the Dirac nodes goes between nearest-neighbor moiré Dirac nodes: i.e., in between the dashed lines in Fig. 4. The series of lattices of twisted bi-layer graphene that are constrained by $m - n = 1$ is therefore consistent with the twist construction for the moiré reciprocal lattice introduced by Bistritzer and MacDonald [7]. In that construction, the displacement (55) coincides with a segment of a honeycomb cell that is at the edge of the first moiré Brillouin zone. Recall that in this case, the cells of the moiré pattern in real space are strictly periodic.

At first sight, on the other hand, bi-layer graphene with commensurate twist angles at integer parameters $m - n > 1$ is not consistent with the Bistritzer-MacDonald twist construction of the reciprocal lattice [7]. By Fig. 4 and (55), applying equal and opposite twists of a Dirac node in graphene by an angle α about the Γ point results in honeycomb supercells in momentum space that include $(m - n)^2$ moiré reciprocal lattice vector in this case. The Bistritzer-MacDonald twist construction in this general case remains physically relevant, however. Applying duality to the $(m - n)^2$ moiré Brillouin zones in the honeycomb supercell indicates that the true Wigner-Seitz unit cell of the bi-layer graphene lattice contains $(m - n)^2$ subcells corresponding to each cell of the moiré pattern. Figure 12 displays the moiré pattern for integer parameters $m = 7$ and $n = 5$. It reveals a moiré subcell at the center of the true Wigner-Seitz unit cell, plus moiré subcells at the center of the edges of the true Wigner-Seitz unit cell. This results, correctly, in $1 + \frac{1}{2}6 = 4$ moiré subcells in each true Wigner-Seitz unit cell. The moiré subcells are notably *not* periodic.

6.2. Inter-Valley Mixing versus Kekulé Spiral Order

The truncated hamiltonian (20) for an electron carrying momentum near the corner of the moiré Brillouin zone reveals that the $K+$ and $K-$ valleys in the different sheets of graphene mix according to the matrix elements $w'_{A-,B+} = w'_1$ and $w'_{A-,A+} = w'_0$. Along the Periodic Moiré Pattern line, $m = n + 1$, nearest-neighbor hopping between the two graphene sheets is described by Figs. 2 and 3. Following expressions (23)-(25), this yields the formula (26) for the matrix element $w'_{A-,B+}$. It is more generally given by

$$w'_1 = - \sum_{(n_1, n_2) \in \text{mWSuc}} \frac{t_{\perp}^{(1)}}{l} (e^{i2\pi/3})^{n_1 + n_2}, \quad (56)$$

where $n_1 \mathbf{a}_1 + n_2 \mathbf{a}_2$ lie inside the moiré Wigner-Seitz unit cell (mWSuc). The matrix element w'_1 is thereby small and of order $t_{\perp}^{(1)}/l$ due to the summation of phase factors that are cube roots of unity.

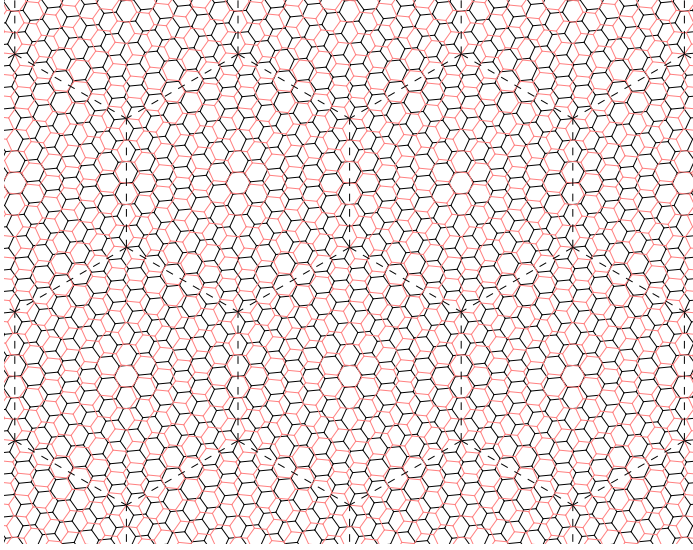


Figure 12. Moiré pattern of two honeycombs twisted by a commensurate angle $\theta = 10.99^\circ$. It corresponds to integer parameters $m = 7$ and $n = 5$. The dashed lines mark the edges of the *true* Wigner-Seitz unit cell, with $l = 109$ A(B) sites per sheet of graphene inside of it.

The field of cube roots of unity $(e^{i2\pi/3})^{n_1+n_2}$ in formula (56) for the inter-valley matrix element $w'_{A-,B+}$ describes a Kekulé spiral over the honeycomb cells of a sheet of graphene. Recent theoretical work predicts incommensurate Kekulé spiral order in magic-angle twisted bi-layer graphene at a filling of $\nu = 2$ electrons or holes per moiré unit cell[18]. Recent scanning-tunnelling microscopy (STM) studies of magic-angle twisted bi-layer graphene have confirmed this prediction[19]. Further, recent STM studies of trilayer graphene at the magic twist angle also find evidence for Kekulé spirals[20]. Such naturally occurring Kekulé spiral order could therefore result in a dramatic increase in the inter-valley mixing according to formula (56) for the matrix element $w'_{A-,B+}$.

7. Conclusions

We have studied a nearest-neighbor electron hopping model for twisted bi-layer graphene. A commensurate twist about a Bernal stack is made, resulting in a super-honeycomb of Bernal stacks. (See Fig. 1.) A mechanism for flat central bands at the magic twist angle is revealed. It is due to optimal level repulsion at the middle of the edge of the moiré Brillouin zone. This result was obtained in the case of periodic moiré patterns with no subcells, in the limit that they are large.

The nearest-neighbor electron hopping model also shows appreciable breaking of valley degeneracy of the flat bands near the magic twist angle. In particular, Fig. 11 shows substantial breaking of valley degeneracy at the M_M point in momentum space, which corresponds to the van Hove singularity. It could lead to correlated insulating states at electron filling such that the chemical potential lies within the split energies

there. This will be investigated in future studies.

7.1. Acknowledgments

The author thanks Eslam Khalaf and Christopher Gutierrez for useful conversations.

Appendix A. Gauge Transformation

The phase factors associated with the off-diagonal A/B and B/A matrix elements (18) can be removed by a gauge transformation. In particular, make the following replacement of the states in the entire hopping hamiltonian, including the diagonal parts, H_{--} and H_{++} , and the off-diagonal parts, H_{-+} and H_{+-} :

$$\begin{aligned} |\mathbf{k} - \mathbf{G}_i, B, -\rangle &\rightarrow e^{+i\mathbf{G}_i \cdot \mathbf{C}_2} |\mathbf{k} - \mathbf{G}_i, B, -\rangle, \\ |\mathbf{k} - \mathbf{G}_j, A, +\rangle &\rightarrow e^{+i\mathbf{G}_j \cdot \mathbf{C}_2} |\mathbf{k} - \mathbf{G}_j, A, +\rangle, \end{aligned} \quad (\text{A.1})$$

and

$$\begin{aligned} |\mathbf{k} - \mathbf{G}_i, A, -\rangle &\rightarrow e^{-i\mathbf{G}_i \cdot \mathbf{C}_3} |\mathbf{k} - \mathbf{G}_i, A, -\rangle, \\ |\mathbf{k} - \mathbf{G}_j, B, +\rangle &\rightarrow e^{-i\mathbf{G}_j \cdot \mathbf{C}_3} |\mathbf{k} - \mathbf{G}_j, B, +\rangle. \end{aligned} \quad (\text{A.2})$$

This results in the replacement

$$\zeta_{\pm}(\mathbf{k} - \mathbf{G}_i) \rightarrow e^{\mp i\mathbf{G}_i \cdot \mathbf{C}_1} \zeta_{\pm}(\mathbf{k} - \mathbf{G}_i) \quad (\text{A.3})$$

of the phase factors for the intra-graphene-sheet matrix elements (13), and in the replacements

$$\begin{aligned} \langle\langle \mathbf{k}_i, A, - | H | \mathbf{k}_j, A, + \rangle\rangle &= - e^{-i(\mathbf{G}_i \cdot \mathbf{C}_3 + \mathbf{G}_j \cdot \mathbf{C}_2)} \cdot \sum_{\delta \mathbf{r}_{A/A}} \frac{t_{\perp}^{(0)}}{l} e^{i[-\mathbf{k}_i \cdot \delta \mathbf{r}_{A/A}(-) + \mathbf{k}_j \cdot \delta \mathbf{r}_{A/A}(+)]} \\ \langle\langle \mathbf{k}_i, A, - | H | \mathbf{k}_j, B, + \rangle\rangle &= - \sum_{\delta \mathbf{r}_{B/A}} \frac{t_{\perp}^{(1)}}{l} e^{i[-\mathbf{k}_i \cdot \delta \mathbf{r}_{B/A}(-) + \mathbf{k}_j \cdot \delta \mathbf{r}_{B/A}(+)]} \\ \langle\langle \mathbf{k}_i, B, - | H | \mathbf{k}_j, A, + \rangle\rangle &= - \sum_{\delta \mathbf{r}_{A/B}} \frac{t_{\perp}^{(1)}}{l} e^{i[-\mathbf{k}_i \cdot \delta \mathbf{r}_{A/B}(-) + \mathbf{k}_j \cdot \delta \mathbf{r}_{A/B}(+)]} \\ \langle\langle \mathbf{k}_i, B, - | H | \mathbf{k}_j, B, + \rangle\rangle &= - e^{+i(\mathbf{G}_i \cdot \mathbf{C}_2 + \mathbf{G}_j \cdot \mathbf{C}_3)} \cdot \sum_{\delta \mathbf{r}_{B/B}} \frac{t_{\perp}^{(0)}}{l} e^{i[-\mathbf{k}_i \cdot \delta \mathbf{r}_{B/B}(-) + \mathbf{k}_j \cdot \delta \mathbf{r}_{B/B}(+)]} \end{aligned} \quad (\text{A.4})$$

of the inter-graphene-sheet matrix elements (18). In the right-hand side of (A.3), we have used the identity $\mathbf{C}_1 + \mathbf{C}_2 + \mathbf{C}_3 = 0$. Above, also, $\mathbf{k}_i = \mathbf{k} - \mathbf{G}_i$ and $\mathbf{k}_j = \mathbf{k} - \mathbf{G}_j$. Notice that this guage transformation consolidates the phase factors on the block-diagonal intra-graphene parts of the hopping hamiltonian in the chiral limit[10], where there is no A/A nor B/B inter-graphene-sheet hopping.

Appendix B. Phase Factors, Quotient Groups

The product of the phase factor $e^{i\mathbf{k} \cdot \mathbf{c}_1(\pm)}$ with (21) $\zeta'_{\pm}(\mathbf{k})$ gives the intra-graphene matrix element (14) $\zeta_{\pm}(\mathbf{k})$. The reduced matrix element $\zeta'_{\pm}(\mathbf{k})$ is periodic over the graphene Brillouin zone, while the phase factor $e^{i\mathbf{k} \cdot \mathbf{c}_1(\pm)}$ is not. Let us compute the phase factor

in twisted bi-layer graphene at momentum $\mathbf{k} = +K_{\bar{M}}\hat{\mathbf{x}}$, where the $K+$ Dirac zero of the $+\alpha$ -rotated sheet of graphene coincides with the $K-$ Dirac zero of the $-\alpha$ -rotated sheet of graphene. (See Fig. 6, red dot in black circle.) In the latter case, the argument of the exponential is imaginary i times the dot product $K_{\bar{M}}\hat{\mathbf{x}} \cdot \mathbf{c}_1(-) = K_{\bar{M}}\hat{\mathbf{x}}(+)\cdot \mathbf{c}_1$, where the notation $\mathbf{v}(\pm)$ means that the vector \mathbf{v} is rotated by $\pm\alpha$. Now observe that $K_{\bar{M}}\hat{\mathbf{x}}(+)= -m\mathbf{d}_2 + n\mathbf{d}_3$. By (10), we thereby obtain $(Ka)(m+n)\frac{\sqrt{3}}{2} = 2\pi(m+n)/3$ times imaginary i for the argument of the exponential, or

$$e^{+iK_{\bar{M}}\hat{\mathbf{x}}\cdot\mathbf{c}_1(-)} = e^{i2\pi(m+n)/3}. \quad (\text{B.1})$$

In the case of the phase factor $e^{+iK_{\bar{M}}\hat{\mathbf{x}}\cdot\mathbf{c}_1(+)}$, on the other hand, the argument of the exponential is imaginary i times the dot product $K_{\bar{M}}\hat{\mathbf{x}} \cdot \mathbf{c}_1(+) = K_{\bar{M}}\hat{\mathbf{x}}(-)\cdot \mathbf{c}_1$. Observe, once more, that $K_{\bar{M}}\hat{\mathbf{x}}(-) = -n\mathbf{d}_2 + m\mathbf{d}_3$. Compared to the previous case, we have swapped m with n . The phase factor in this case is thereby given by the phase factor in the previous case (B.1).

The other phase factor that appears in the nearest-neighbor electron hopping model for bi-layer graphene at commensurate twist angles is linked to the inter-graphene-sheet matrix elements between A sites and B sites (18). In the case of hopping from a B site in the plus-rotated sheet of graphene to an A site in the minus-rotated sheet of graphene, for example, the phase factor is given by $e^{i\mathbf{G}_-\cdot\mathbf{C}_3}e^{-i\mathbf{G}_+\cdot\mathbf{C}_3}$, where $\mathbf{G}_- = n_1^{(-)}\mathbf{B}_1 + n_2^{(-)}\mathbf{B}_2$ and $\mathbf{G}_+ = n_1^{(+)}\mathbf{B}_1 + n_2^{(+)}\mathbf{B}_2$ are moiré reciprocal lattice vectors. Using expressions (4) and (5) for the moiré A-B displacements \mathbf{C}_i (see Fig. 1) and the primitive vectors \mathbf{B}_j of the moiré reciprocal lattice, we get the result $e^{i\mathbf{G}_{\pm}\cdot\mathbf{C}_1} = (e^{-i2\pi/3})^{n_1^{(\pm)}+n_2^{(\pm)}}$. Next, using the identity $\mathbf{C}_3 = \mathbf{C}_1 + \mathbf{C}_3 - \mathbf{C}_1 = \mathbf{C}_1 - \mathbf{A}_2$, we get the same result for $e^{i\mathbf{G}_{\pm}\cdot\mathbf{C}_3}$. The net phase factor is therefore

$$e^{i\mathbf{G}_-\cdot\mathbf{C}_3}e^{-i\mathbf{G}_+\cdot\mathbf{C}_3} = (e^{-i2\pi/3})^{n_1^{(-)}+n_2^{(-)}}(e^{+i2\pi/3})^{n_1^{(+)}+n_2^{(+)}}. \quad (\text{B.2})$$

Importantly, this result yields that the net phase factor is *unity* if $(n_1^{(-)} + n_2^{(-)}) \bmod 3 = (n_1^{(+)} + n_2^{(+)}) \bmod 3$. In other words, the net phase factor (B.2) is unity when \mathbf{G}_- and \mathbf{G}_+ lie in the *same* 3-fold sublattice of the triangular moiré reciprocal lattice. These are (a) sites with $(n_1 + n_2) \bmod 3 = 1$, (b) sites with $(n_1 + n_2) \bmod 3 = 2$, and (c) sites with $(n_1 + n_2) \bmod 3 = 0$. Such a and b sites form a honeycomb on the original triangular moiré reciprocal lattice, with c sites at the centers of the honeycomb cells.

Last, Fig. 5 shows the first Brillouin zones of the plus-rotated and the minus-rotated sheets of graphene, $1BZ(+)$ and $1BZ(-)$, respectively. Notice that both Brillouin zones contain the *same* moiré reciprocal lattice vectors, $\{\mathbf{G}_0, \mathbf{G}_1, \dots, \mathbf{G}_{l-1}\}$, with $l = 61$ in this particular case. The periodic structure of the first Brillouin zone $1BZ(+)$ displayed by Fig. 5 means that a *quotient group* exists that is composed of the l moiré reciprocal lattice vectors that it contains. Summation of two elements in the group is defined up to the periodicity: $\mathbf{G}_+ + \mathbf{G}'_+ \rightarrow (\mathbf{G}_+ + \mathbf{G}'_+) \bmod 1BZ(+)$. The quotient group is therefore equal to $Z^2(\text{moiré})/Z^2(\text{graphene+})$, where $Z^2(\text{moiré})$ is the moiré reciprocal lattice, and where $Z^2(\text{graphene+})$ is the reciprocal lattice of the plus-rotated sheet of graphene. A related group exists based on the minus-rotated sheet of graphene, where $1BZ(+)$ is replaced by $1BZ(-)$. (See Fig. 5.)

The above quotient groups emerge when momentum is added to bi-layer graphene at commensurate twist angles. In particular, notice that the difference between $(\mathbf{G}_+ + \Delta\mathbf{G}) \bmod 1BZ(+)$ and $(\mathbf{G}_- + \Delta\mathbf{G}) \bmod 1BZ(-)$ is *not* necessarily equal to the difference between \mathbf{G}_+ and \mathbf{G}_- . This is a result of the twist angle. However, the previous phase factor (B.2) does indeed remain the same:

$$e^{i(\mathbf{G}_- + \Delta\mathbf{G}) \cdot \mathbf{C}_3} e^{-i(\mathbf{G}_+ + \Delta\mathbf{G}) \cdot \mathbf{C}_3} = e^{i\mathbf{G}_- \cdot \mathbf{C}_3} e^{-i\mathbf{G}_+ \cdot \mathbf{C}_3}. \quad (\text{B.3})$$

This property can be exploited when computing the previous phase factor after the addition of a moiré reciprocal lattice vector $\Delta\mathbf{G}$. (See Fig. 8 and the end of subsection 4.2.)

Appendix C. Inter-Graphene Matrix Elements: 3-Fold Rotation Symmetry, Geometric Series Sums

Below, we shall compute explicitly the inter-graphene-sheet matrix elements that appear in the four-fold degenerate perturbation theory analysis found in section 4. In particular, we shall confine ourselves to twisted bi-layer graphene at integer parameters $m = n + 1$. The nearest-neighbor hopping links in between the two sheets of graphene have the “hexagon” form depicted by Figs. 2 and 3 in such case. Also, the nearest-neighbor hopping model hamiltonian has the form (19), with matrix elements (13) and (18) in momentum space for H_{--} , H_{-+} , etc. . The simplest hopping model shall be assumed: *all* of the nearest-neighbor hopping matrix elements between the twisted graphene sheets are unique, and they are given by $-t_{\perp}^{(0)}$ and $-t_{\perp}^{(1)}$. Here, the superscript 0 refers to A-A links between sheets of graphene, while the superscript 1 refers to the corresponding A-B links.

Appendix C.1. Application of 3-Fold and 6-Fold Rotation Symmetry

Figure 1 reveals that the twist centers at $B+/A-$ Bernal stacks show 6-fold rotation symmetry. It becomes useful to exploit this symmetry when computing the corresponding matrix element (18) $\langle\langle \mathbf{k}_i, A, - | H | \mathbf{k}_j, B, + \rangle\rangle$. In particular, the sum over inter-graphene links can be re-expressed as

$$h_{A-,B+} = \frac{t_{\perp}^{(1)}}{l} \left[1 + 2 \operatorname{Re} \sum_{n_1=1}^n \sum_{n_2=0}^{n_1-1} \left(e^{i[-\mathbf{k}_i \cdot \delta\mathbf{r}_{B/A}(-) + \mathbf{k}_j \cdot \delta\mathbf{r}_{B/A}(+)]} + e^{i[-\mathbf{k}_i \cdot \delta\mathbf{r}'_{B/A}(-) + \mathbf{k}_j \cdot \delta\mathbf{r}'_{B/A}(+)]} + e^{i[-\mathbf{k}_i \cdot \delta\mathbf{r}''_{B/A}(-) + \mathbf{k}_j \cdot \delta\mathbf{r}''_{B/A}(+)]} \right) \right], \quad (\text{C.1})$$

with 3-fold-symmetric displacements from the Bernal stack

$$\begin{aligned} \delta\mathbf{r}_{B/A}(\pm) &= n_1 \mathbf{a}_1(\pm) + n_2 \mathbf{a}_2(\pm), \\ \delta\mathbf{r}'_{B/A}(\pm) &= n_1 \mathbf{a}_2(\pm) + n_2 \mathbf{a}_3(\pm), \\ \delta\mathbf{r}''_{B/A}(\pm) &= n_1 \mathbf{a}_3(\pm) + n_2 \mathbf{a}_1(\pm). \end{aligned} \quad (\text{C.2})$$

The phase factors and minus signs in (18) have been suppressed above in (C.1). Figure 2 shows the $B+/A-$ links between the twisted sheets of graphene within a moiré Wigner-Seitz cell. The sums over the integers n_1 and n_2 in (C.1) represent the sector including 90° up from the twist center to 150° from the twist center.

Figure 1 also reveals that the twist centers of $A+/A-$ links between twisted sheets of graphene show instead only 3-fold rotation symmetry. This symmetry can once again be exploited, however, to compute the corresponding matrix element (18) $\langle\langle \mathbf{k}_i, A, -|H|\mathbf{k}_j, A, + \rangle\rangle$. Figure 3 displays the $A+/A-$ links between the twisted sheets of graphene inside a moiré Wigner-Seitz cell. Notice the nucleus of 6 links in the inner triangle, plus 3 trapezoids adjacent to the inner triangle, in addition to 3 outer triangles adjacent to the trapezoids. Also observe that a trapezoid plus an adjacent outer triangle form a parallelogram! By exploiting 3-fold rotation symmetry, the sum on the right-hand side of the expression (18) for the matrix element $\langle\langle \mathbf{k}_i, A, -|H|\mathbf{k}_j, A, + \rangle\rangle$ becomes

$$h_{A-,A+}^{(\text{ncls})} = \frac{t_\perp^{(0)}}{l} \sum_{(m_1, m_2)=(0, -2), (1, 0)} (e^{i[-\mathbf{k}_i \cdot \delta \mathbf{r}_{A/A}(-) + \mathbf{k}_j \cdot \delta \mathbf{r}_{A/A}(+)]} + e^{i[-\mathbf{k}_i \cdot \delta \mathbf{r}'_{A/A}(-) + \mathbf{k}_j \cdot \delta \mathbf{r}'_{A/A}(+)]} + e^{i[-\mathbf{k}_i \cdot \delta \mathbf{r}''_{A/A}(-) + \mathbf{k}_j \cdot \delta \mathbf{r}''_{A/A}(+)]}), \quad (\text{C.3})$$

plus

$$h_{A-,A+}^{(\text{hxgn})} = \frac{t_\perp^{(0)}}{l} \sum_{n_3=0}^{n-2} \sum_{n_1=0}^{n+1} (e^{i[-\mathbf{k}_i \cdot \delta \mathbf{r}_{A/A}(-) + \mathbf{k}_j \cdot \delta \mathbf{r}_{A/A}(+)]} + e^{i[-\mathbf{k}_i \cdot \delta \mathbf{r}'_{A/A}(-) + \mathbf{k}_j \cdot \delta \mathbf{r}'_{A/A}(+)]} + e^{i[-\mathbf{k}_i \cdot \delta \mathbf{r}''_{A/A}(-) + \mathbf{k}_j \cdot \delta \mathbf{r}''_{A/A}(+)]}) \quad (\text{C.4})$$

if $n > 1$, with 3-fold-symmetric displacements from the twist center

$$\begin{aligned} \delta \mathbf{r}_{A/A}(\pm) &= m_1 \mathbf{c}_1(\pm) + m_2 \mathbf{c}_2(\pm), \\ \delta \mathbf{r}'_{A/A}(\pm) &= m_1 \mathbf{c}_2(\pm) + m_2 \mathbf{c}_3(\pm), \\ \delta \mathbf{r}''_{A/A}(\pm) &= m_1 \mathbf{c}_3(\pm) + m_2 \mathbf{c}_1(\pm). \end{aligned} \quad (\text{C.5})$$

Again, the phase factors and minus signs in (18) have been suppressed above in (C.3) and in (C.4). Also above in (C.5), m_1 and m_2 are integers that satisfy $(m_1 + m_2) \bmod 3 = 1$ on the A sites, while the integers n_3 and n_1 denote the column and row, respectively, of an A site in the previous parallelogram. This parallelogram is the union of the trapezoid adjacent and to the right of the inner triangle shown in Fig. 3 with the outer triangle on top and adjacent to the trapezoid. The location of an A-site in the parallelogram is (C.5) $\delta \mathbf{r}_{A/A} = m_1 \mathbf{c}_1 + m_2 \mathbf{c}_2$. The relationship between (m_1, m_2) and the column-row integers n_3 and n_1 is then

$$(m_1, m_2) \cdot (\mathbf{c}_1, \mathbf{c}_2) = (1, -3) \cdot (\mathbf{c}_1, \mathbf{c}_2) + (n_3, n_1) \cdot (\mathbf{a}_3, \mathbf{a}_1). \quad (\text{C.6})$$

Above, $(1, -3)$ are the coordinates for the bottom-left corner of the parallelogram. Substituting in the identities $\mathbf{a}_3 = \mathbf{c}_1 - \mathbf{c}_2$ and $\mathbf{a}_1 = \mathbf{c}_2 - \mathbf{c}_3 = \mathbf{c}_1 + 2\mathbf{c}_2$ above then yields

$$(m_1, m_2) = (1, -3) + n_3(1, -1) + n_1(1, 2)$$

$$= (1 + n_3 + n_1, -3 - n_3 + 2n_1). \quad (\text{C.7})$$

As a consistency check, notice that the number of terms in the the matrix elements (C.3) plus (C.4) is $3n(n+1)$, which is equal to $l-1$.

Appendix C.2. w'_0 and w'_1

At in-going and out-going momenta $\mathbf{k}_j = K_{\bar{M}}\hat{\mathbf{x}} = \mathbf{k}_i$ (see the red-dot-in-black-circle, Fig. 6), minus expression (C.1) for the A-B matrix element reduces to expression (26) for w'_1 in the text:

$$w'_1 = -(t_{\perp}^{(1)}/l)(1 + 6 \text{Re } S'_1), \quad (\text{C.8})$$

with series sum

$$\begin{aligned} S'_1 &= \sum_{n_1=1}^n \sum_{n_2=0}^{n_1-1} (e^{i2\pi/3})^{n_1+n_2} \\ &= \sum_{n_1=1}^n (e^{i2\pi/3})^{n_1} \frac{1 - (e^{i2\pi/3})^{n_1}}{1 - e^{i2\pi/3}} \\ &= \frac{1}{1 - e^{i2\pi/3}} \left[e^{i2\pi/3} \frac{1 - (e^{i2\pi/3})^n}{1 - e^{i2\pi/3}} - \text{c.c.} \right]. \end{aligned} \quad (\text{C.9})$$

Above, we have used the result

$$\begin{aligned} S_{0,m}(z) &= 1 + z + z^2 + \dots + z^m \\ &= \frac{1 - z^{m+1}}{1 - z} \end{aligned} \quad (\text{C.10})$$

for the summation of a geometric series. After some manipulation, we arrive at the result

$$S'_1 = -\frac{1 - \sqrt{3}i}{3} \left(\frac{1}{2} + \cos \left[\frac{2\pi}{3}(n-1) \right] \right) \quad (\text{C.11})$$

for the series sum. Substitution in (C.8) thereby yields the final result

$$w'_1 = 2 \frac{t_{\perp}^{(1)}}{l} \cos \left[\frac{2\pi}{3}(n-1) \right] \quad (\text{C.12})$$

for the matrix element.

Also, at the same in-going and out-going momenta, the A-A matrix elements above, (C.3) and (C.4), reduce to

$$h_{A-,A+}^{(\text{ncls})} = \frac{1}{l} \sum_{(m_1, m_2) = (0, -2), (1, 0)} t_{\perp}^{(0)} \zeta_{A/A}^{(m_1, m_2)}(\mathbf{k}) \quad (\text{C.13})$$

and

$$h_{A-,A+}^{(\text{hxgn})} = \frac{1}{l} \sum_{n_3=0}^{n-2} \sum_{n_1=0}^{n+1} t_{\perp}^{(0)} \zeta_{A/A}^{(m_1, m_2)}(\mathbf{k}), \quad (\text{C.14})$$

where $\zeta_{A/A}^{(m_1, m_2)}(\mathbf{k})$ is a 3-fold-rotation-symmetric phase factor given by (28)-(30), with $\mathbf{k} = K_{\bar{M}}\hat{\mathbf{x}}$. It is shown in the text that the latter reduces to expression (32), which when

substituted into expressions (C.13) and (C.14) above for $h_{A-,A+}^{(\text{ncls})}$ and $h_{A-,A+}^{(\text{hxgn})}$ equal zero because of 3-fold rotation symmetry.

We must therefore compute the gradient of the phase factor (28) $\zeta_{A/A}^{(m_1, m_2)}(\mathbf{k})$ at in-going and out-going momenta $\mathbf{k}_j = K_{\bar{M}}\hat{\mathbf{x}} = \mathbf{k}_i$:

$$\begin{aligned} \nabla_{\mathbf{k}} \zeta_{A/A}^{(m_1, m_2)}|_{K_{\bar{M}}\hat{\mathbf{x}}} &= i[\delta\mathbf{c}_0(m_1, m_2)e^{iK_{\bar{M}}\hat{\mathbf{x}} \cdot \delta\mathbf{c}_0(m_1, m_2)} + \\ &\quad \delta\mathbf{c}_+(m_1, m_2)e^{iK_{\bar{M}}\hat{\mathbf{x}} \cdot \delta\mathbf{c}_+(m_1, m_2)} + \\ &\quad \delta\mathbf{c}_-(m_1, m_2)e^{iK_{\bar{M}}\hat{\mathbf{x}} \cdot \delta\mathbf{c}_-(m_1, m_2)}]. \end{aligned} \quad (\text{C.15})$$

Above, $\delta\mathbf{c}_0(m_1, m_2)$, $\delta\mathbf{c}_+(m_1, m_2)$, and $\delta\mathbf{c}_-(m_1, m_2)$, and the corresponding dot products with $K_{\bar{M}}\hat{\mathbf{x}}$ are given by expressions (29), (30), and (31) in the text. Direct calculation yields the result

$$\begin{aligned} \nabla_{\mathbf{k}} \zeta_{A/A}^{(m_1, m_2)}|_{K_{\bar{M}}\hat{\mathbf{x}}} &= 3(\sin \alpha) a(e^{-i2\pi/3})^{m_1 - m_2} \cdot \\ &\quad \cdot (e^{+i2\pi/3} m_1 + e^{-i2\pi/3} m_2)(\hat{\mathbf{x}} - i\hat{\mathbf{y}}). \end{aligned} \quad (\text{C.16})$$

We therefore have the matrix element of the form $w_0 = w_0^{(1)}(\delta k_x - i\delta k_y)$, with group velocity of the form $w_0'^{(1)} = w_{0, \text{ncls}}'^{(1)} + w_{0, \text{hxgn}}'^{(1)}$. By (C.13) and (C.16) above, the contribution from the “nucleus” to the group velocity is $w_{0, \text{ncls}}'^{(1)} = 3(\sin \alpha) a t_{\perp}^{(0)}/l$. Along the Periodic Moiré Pattern line, $m = n + 1$, we have $2\sin \alpha = 1/\sqrt{l}$, and therefore $w_{0, \text{ncls}}'^{(1)} = (3/2) a t_{\perp}^{(0)}/l^{3/2}$.

Also, by (C.14) and (C.16) above, the contribution from the “hexagon” to the group velocity is $w_{0, \text{hxgn}}'^{(1)} = -3(\sin \alpha) a t_{\perp}^{(0)} S'_0/l$, with summation

$$S'_0 = \sum_{n_3=0}^{n-2} \sum_{n_1=0}^{n+1} (e^{i2\pi/3})^{m_2 - m_1} (e^{i2\pi/3} m_1 + e^{-i2\pi/3} m_2). \quad (\text{C.17})$$

Next, call $z_1 = e^{-i2\pi/3}$ and $z_2 = e^{+i2\pi/3}$. Observe that we then have the identity

$$\begin{aligned} S'_0 &= \sum_{n_3=0}^{n-2} \sum_{n_1=0}^{n+1} z_1^{m_1} z_2^{m_2} (z_2 m_1 + z_1 m_2) \\ &= z_1 z_2 \left(\frac{\partial}{\partial z_1} + \frac{\partial}{\partial z_2} \right) \sum_{n_3=0}^{n-2} \sum_{n_1=0}^{n+1} z_1^{m_1} z_2^{m_2}. \end{aligned} \quad (\text{C.18})$$

By (C.7), the new summation above acted upon by the partial derivatives is then

$$\begin{aligned} S''_0 &= \sum_{n_3=0}^{n-2} \sum_{n_1=0}^{n+1} z_1^{1+n_3+n_1} z_2^{-3-n_3+2n_1} \\ &= z_1^1 z_2^{-3} \sum_{n_3=0}^{n-2} (z_1/z_2)^{n_3} \sum_{n_1=0}^{n+1} (z_1 z_2^2)^{n_1} \\ &= z_1 z_2^{-3} \cdot \frac{1 - (z_1/z_2)^{n-1}}{1 - (z_1/z_2)} \cdot \frac{1 - (z_1 z_2^2)^{n+2}}{1 - z_1 z_2^2}. \end{aligned} \quad (\text{C.19})$$

Substituting this expression for S''_0 into the summation in expression (C.18) for S'_0 yields the result

$$S'_0 = 3z_1 \left(\frac{1 - z_2^{n-1}}{1 - z_2} \right)^2 \frac{1 - z_1}{1 - z_2}$$

$$-z_1 \frac{z_2^{n-1} - z_1^{n-1}}{(1-z_2)^2} [(n-4)z_2 - (n+5)]. \quad (\text{C.20})$$

The second term above dominates at large n , where we get the limiting result

$$\lim_{n \rightarrow \infty} S'_0 = nz_1(2i \sin[2\pi(n-1)/3])/(1-z_2). \quad (\text{C.21})$$

Using the identity $1-z_2 = i\sqrt{3}z_1$ thereby yields the result

$$\lim_{n \rightarrow \infty} S'_0 = \frac{2}{\sqrt{3}}n \sin[2\pi(n-1)/3]. \quad (\text{C.22})$$

In conclusion, at large n , the group velocity is given by the above “hexagon” contribution:

$$\lim_{n \rightarrow \infty} w'_{0,\text{hxgn}} = -3(\sin \alpha) \frac{a t_{\perp}^{(0)}}{l} \cdot \frac{2}{\sqrt{3}}n \sin\left[\frac{2\pi}{3}(n-1)\right]. \quad (\text{C.23})$$

Using the limit $\lim_{n \rightarrow \infty} \sin \alpha = (2\sqrt{3}n)^{-1}$ for half the twist angle along the Periodic Moiré Pattern line then yields the final result for the group velocity at large n :

$$\lim_{n \rightarrow \infty} w'_{0,\text{hxgn}} = -\frac{a t_{\perp}^{(0)}}{l} \sin\left[\frac{2\pi}{3}(n-1)\right]. \quad (\text{C.24})$$

Appendix C.3. w_0 and w_1

And at in-going and out-going momenta $\mathbf{k}_j = M_M \hat{\mathbf{y}} = \mathbf{k}_i$ (see Figs. 6 and 8), minus expression (C.1) for the A-B matrix element reduces to expression (40) for w_1 in the text:

$$w_1 = -\frac{t_{\perp}^{(1)}}{l} [1 + 2 \operatorname{Re} \sum_{n_1=1}^n \sum_{n_2=0}^{n_1-1} (z_0^{-n_2} + z_0^{n_2-n_1} + z_0^{n_1})], \quad (\text{C.25})$$

where $z_0 = \exp[i(2\pi/3)\sqrt{3}(\sin \theta)]$. The sum due to the first term inside the parentheses above is

$$\begin{aligned} S_1(1) &= \sum_{n_1=1}^n \sum_{n_2=0}^{n_1-1} z_0^{-n_2} \\ &= n + (n-1)z_0^{-1}(n-2)z_0^{-2} + \dots + z_0^{-(n-1)} \\ &= z_0^{-(n-1)}(1 + 2z_0 + 3z_0^2 + \dots + nz_0^{n-1}). \end{aligned} \quad (\text{C.26})$$

Hence, the sum above is obtained from the derivative of the sum $S_{0,n}(z_0)$ of the geometric series (C.10) by

$$S_1(1) = \frac{1}{z_0^{n-1}} \frac{dS_{0,n}}{dz_0}, \quad (\text{C.27})$$

with

$$\frac{dS_{0,n}}{dz_0} = \frac{1}{(1-z_0)^2} [1 - (n+1)z_0^n + nz_0^{n+1}]. \quad (\text{C.28})$$

Next, the sum due to the second term inside the parentheses above in (C.25) is

$$\begin{aligned}
 S_1(2) &= \sum_{n_1=1}^n z_0^{-n_1} \sum_{n_2=0}^{n_1-1} z_0^{+n_2} \\
 &= \sum_{n_1=1}^n z_0^{-n_1} \frac{1 - z_0^{n_1}}{1 - z_0} \\
 &= \frac{1}{1 - z_0} \left[\frac{1 - z_0^{-(n+1)}}{1 - z_0^{-1}} - 1 - n \right].
 \end{aligned} \tag{C.29}$$

Last, the sum due to the third term inside the parentheses above in (C.25) is

$$\begin{aligned}
 S_1(3) &= \sum_{n_1=1}^n z_0^{n_1} \sum_{n_2=0}^{n_1-1} 1 \\
 &= z_0 + 2z_0^2 + 3z_0^3 + \dots + nz_0^n.
 \end{aligned} \tag{C.30}$$

It is related to the derivative (C.28) of the sum $S_{0,n}(z_0)$ of the geometric series (C.10) by

$$S_1(3) = z_0 \frac{dS_{0,n}}{dz_0}. \tag{C.31}$$

It is z_0^n times the series sum (C.27) $S_1(1)$ from the first term.

The final sum in w_1 above (C.25) is $2 \operatorname{Re}[S_1(1) + S_1(2) + S_1(3)]/l$. It can be evaluated in simple form at large n . In particular, from (1) and (2), we identify the useful limits

$$l \rightarrow 3 \left(n + \frac{1}{2} \right)^2 \quad \text{and} \quad z_0 \rightarrow \exp \left(\frac{i}{n + \frac{1}{2}} \frac{2\pi}{3} \right) \tag{C.32}$$

as n approaches infinity. Plugging in these limits into the expressions above then yields the final result for the matrix element:

$$\lim_{n \rightarrow \infty} w_1 = -\frac{3}{2\pi} \left(\frac{1}{\sqrt{3}} + \frac{3}{2\pi} \right) t_{\perp}^{(1)} \cong -0.5036 t_{\perp}^{(1)}. \tag{C.33}$$

Note that it is important here to plug in the large- n limit $1 - z_0 \rightarrow -(i/n)(2\pi/3)$ in the denominators of the above expressions, (C.27), (C.28), (C.29) and (C.31), for the sums $S_1(1)$, $S_1(2)$, and $S_1(3)$.

Last, at the same in-going and out-going momenta, the A-A matrix elements above, (C.3) and (C.4), reduce to expressions (C.13) and (C.14) in terms of the 3-fold rotation symmetric phase factor (28)-(30) $\zeta_{A/A}^{(m_1, m_2)}(\mathbf{k})$, but evaluated at momentum $\mathbf{k} = M_M \hat{\mathbf{y}}$ instead. It is given by expression (43) in the text. Then by (C.13), we get the following contribution to the A-A matrix element from the “nucleus”:

$$w_{0,\text{ncls}} = -t_{\perp}^{(0)} (3z_0^{2/3} + 2z_0^{-1/3} + z_0^{-4/3})/l. \tag{C.34}$$

Also, by (C.14) above and (43) in the text, the contribution from the “hexagon” to the A-A matrix element has the form $w_{0,\text{hxgn}} = -t_{\perp}^{(0)} S_0/l$, with sum

$$S_0 = \sum_{n_3=0}^{n-2} \sum_{n_1=0}^{n+1} [(z_0^{1/3})^{2m_1-m_2} + (z_0^{1/3})^{-(m_1+m_2)} + (z_0^{1/3})^{2m_2-m_1}]. \tag{C.35}$$

By (C.7), the exponents above are:

$$\begin{aligned} 2m_1 - m_2 &= 5 + 3n_3, \\ m_1 + m_2 &= -2 + 3n_1, \\ 2m_2 - m_1 &= -7 - 3n_3 + 3n_1. \end{aligned} \tag{C.36}$$

The sum due to the first term in (C.35) is then

$$\begin{aligned} S_0(1) &= \sum_{n_3=0}^{n-2} \sum_{n_1=0}^{n+1} z_0^{\frac{5}{3}} z_0^{n_3} \\ &= (n+2) z_0^{5/3} \frac{1 - z_0^{n-1}}{1 - z_0}, \end{aligned} \tag{C.37}$$

the sum due to the second term in (C.35) is then

$$\begin{aligned} S_0(2) &= \sum_{n_3=0}^{n-2} \sum_{n_1=0}^{n+1} z_0^{\frac{2}{3}} z_0^{-n_1} \\ &= (n-1) z_0^{2/3} \frac{1 - z_0^{-(n+2)}}{1 - z_0^{-1}}, \end{aligned} \tag{C.38}$$

and the sum due to the third term in (C.35) is then

$$\begin{aligned} S_0(3) &= z_0^{-7/3} \sum_{n_3=0}^{n-2} z_0^{-n_3} \sum_{n_1=0}^{n+1} z_0^{n_1} \\ &= z_0^{-7/3} \frac{1 - z_0^{-(n-1)}}{1 - z_0^{-1}} \frac{1 - z_0^{n+2}}{1 - z_0}. \end{aligned} \tag{C.39}$$

Figure 9 in the text demonstrates that the present matrix element $w_{0,\text{ncls}} + w_{0,\text{hxgn}}$ takes the form $w_0 = w_0^{(0)} e^{i\alpha}$ at large n , where $w_0^{(0)}$ is real. Also, direct calculation of $S_0 = S_0(1) + S_0(2) + S_0(3)$ yields that the large- n limit for the present matrix element, $\lim_{n \rightarrow \infty} w_0$, coincides with the corresponding limit (C.33) for w_1 , but with the replacement $t_{\perp}^{(1)} \rightarrow t_{\perp}^{(0)}$. Last, notice that the previous phase factor $e^{i\alpha}$ clearly contains the first-order correction by the twist angle to the matrix element w_0 in the limit of large n .

- [1] Y. Cao, V. Fatemi, S. Fang, K. Watanabe, T. Taniguchi, E. Kaxiras, and P. Jarillo-Herrero, “Unconventional superconductivity in magic-angle graphene superlattices”, *Nature* **556**, 43 (2018).
- [2] Y. Cao, V. Fatemi, A. Demir, S. Fang, S.L. Tomarken, J.Y. Luo, J.D. Sanchez-Yamagishi, K. Watanabe, T. Taniguchi, E. Kaxiras, R.C. Ashoori, and P. Jarillo-Herrero, “Correlated insulator behavior at half-filling in magic-angle graphene superlattices”, *Nature* **556**, 80 (2018).
- [3] X. Lu, P. Stepanov, W. Yang, M. Xie, M. Ali Aamir, I. Das, C. Urgell, K. Watanabe, T. Taniguchi, G. Zhang, A. Bachtold, A.H. MacDonald, and D.K. Efetov, “Superconductors, Orbital Magnets and Correlated States in Magic-Angle Bilayer Graphene”, *Nature* **574**, 653 (2019).
- [4] Y. Saito, J. Ge, K. Watanabe, T. Taniguchi, and A.F. Young, “Independent superconductors and correlated insulators in twisted bilayer graphene”, *Nature Physics* **16**, 926 (2020).
- [5] J.M.B. Lopes dos Santos, N.M.R. Peres, and A.H. Castro Neto, “Graphene Bilayer with a Twist: Electronic Structure”, *Phys. Rev. Lett.* **99**, 256802 (2007).
- [6] E. Suarez Morell, J.D. Correa, P. Vargas, M. Pacheco, and Z. Barticevic, “Flat Bands in Slightly Twisted Bilayer Graphene: Tight-binding Calculations”, *Phys. Rev. B* **82**, 121407(R) (2010).
- [7] R. Bistritzer and A.H. MacDonald, “Moiré bands in twisted double-layer graphene”, *Proc. Natl. Acad. Sci. USA* **108**, 12233 (2011).
- [8] J.M. Campanera, G. Savini, I. Suarez-Martinez, and M.I. Heggie, “Density Functional Calculations on the Intricacies of Moiré Patterns on Graphite”, *Phys. Rev. B* **75**, 235449 (2007).
- [9] G. Trambly de Laissardiere, D. Mayou, and L. Magaud, “Localization of Dirac Electrons in Rotated Graphene Bilayers”, *Nano Lett.* **10**, 804 (2010).
- [10] G. Tarnopolsky, A.J. Kruchkov, and A. Vishwanath, “Origin of Magic Angles in Twisted Bilayer Graphene”, *Phys. Rev. Lett.* **122**, 106405 (2019).
- [11] S. Carr, D. Massatt, S.B. Torrisi, P. Cazeaux, M. Luskin, and E. Kaxiras, “Relaxation and Domain Formation in Incommensurate Two-Dimensional Heterostructures”, *Phys. Rev. B* **98**, 224102 (2018).
- [12] H. Yoo, R. Engelke, S. Carr, S. Fang, K. Zhang, P. Cazeaux, S.H. Sung, R. Hovden, A.W. Tsen, T. Taniguchi, K. Watanabe, G.-C. Yi, M. Kim, M. Luskin, E.B. Tadmor, E. Kaxiras, and P. Kim, “Atomic and Electronic Reconstruction at the Van der Waals Interface in Twisted Bilayer Graphene”, *Nat. Mat.* **18**, 448 (2019).
- [13] F. Guinea and N.R. Walet, “Continuum Models for Twisted Bilayer Graphene: Effect of Lattice Deformation and Hopping Parameters”, *Phys. Rev. B* **99**, 205134 (2019).
- [14] S. Carr, S. Fang, Z. Zhu, and E. Kaxiras, “Exact Continuum model for Low-Energy Electronic States of Twisted Bilayer Graphene”, *Phys. Rev. Research* **1**, 013001 (2019).
- [15] N.R. Walet and F. Guinea, “The Emergence of One-Dimensional Channels in Marginal-Angle Twisted Bilayer Graphene”, *2D Mater.* **7**, 015023 (2020).
- [16] N. Leconte, S. Javvaji, J. An, A. Samudrala, and J. Jung, “Relaxation Effects in Twisted Bilayer Graphene: A Multiscale Approach”, *Phys. Rev. B* **106**, 115410 (2022).
- [17] Y. Xie, B. Lian, B. Jäck, X. Liu, C.-L. Chiu, K. Watanabe, T. Taniguchi, B.A. Bernevig, and A. Yazdani, “Spectroscopic signatures of many-body correlations in magic-angle twisted bilayer graphene”, *Nature* **572**, 101 (2019).
- [18] Y.H. Kwan, G. Wagner, T. Soejima, M.P. Zaletel, S.H. Simon, S.A. Parameswaran, and N. Bultinck, “Kekule Spiral Order at All Nonzero Integer Fillings in Twisted Bilayer Graphene”, *Phys. Rev. X* **11**, 041063 (2021).
- [19] K.P. Nuckolls, R.L. Lee, M. Oh, D. Wong, T. Soefima, J.P. Hong, D. Calugaru, J. Herzog-Arbeitman, B.A. Bernevig, K. Watanabe, T. Taniguchi, N. Regnault, M.P. Zaletel, and A. Yazdani, “Quantum Textures of the Many-Body Wavefunction in Magic-Angle Graphene”, *Nature* **620**, 525 (2023).
- [20] H. Kim, Y. Choi, E. Lantagne-Hurtubise, C. Lewandowski, A. Thomson, L. Kong, H. Zhou, E. Baum, Y. Zhang, L. Holleis, K. Watanabe, T. Taniguchi, A.F. Young, J. Alicea, S. Nadj-Perge, “Imaging Inter-Valley Coherent Order in Magic-Angle Twisted Trilayer Graphene”, *Nature* **623**, 942 (2023).